RSC Advances

PAPER

View Article Online
View Journal | View Issue

Cite this: *RSC Adv.*, 2026, **16**, 2504

Functionalized carbon nanotubes for selective lithium recovery from spent lithium-ion batteries: a sustainable approach to resource recycling

Mohamed E. Eissa,*[a] Mohamed Abdel-Megid,[a] Bahig M. Atia,[b] Mohamed A. Gado,[b] Mohamed F. Cheira,[b] Taha F. Hassanein*[c] and Haeam A. Abdelmonem[d]

The intensive use of lithium-ion batteries (LIBs) has led to a surge in battery waste, which is a valuable secondary resource for metal recovery. Discarded LIBs, rich in critical metals like lithium and cobalt, offer a concentrated and economically attractive source, addressing supply limitations and environmental protection. The current study presents a novel, low-cost method for selectively recovering lithium ions from both synthetic solutions and LIB waste. Using a newly created adsorbent, mesoporous carbon nanotubes functionalized with aminomethylenephosphonic acid (CNT–AMP), lithium ions were selectively extracted. Extensive characterization of the structural and functional features of CNT–AMP and/or CNT–AMP/Li was carried out utilizing a variety of techniques, including FT-IR, XPS, BET, magnetization investigations, TEM, ^{1}H-NMR, ^{13}C-NMR, and GC-MS. The ideal lithium recovery (299 mg g^{-1}) was obtained at 500 mg L^{-1} lithium ions, 0.08 g CNT–AMP, pH 12, 25 °C, and 100 minutes of contact time. The adsorption behavior was highly consistent with the Langmuir and D–R models, indicating that chemisorption is the primary driving force behind the process. In an ideal setting, the recovery procedure produced 99.5% pure lithium carbonate (Li_2CO_3), which is confirmed by XRD and SEM, with a recovery efficiency of 95.76%. The results demonstrate that CNT–AMP can be utilized as a high-performance adsorbent for the sustainable recovery of lithium as a valuable recycling metal from battery waste. This helps conserve resources and promote environmental sustainability.

Received 4th October 2025
Accepted 29th December 2025

DOI: 10.1039/d5ra07566a

rsc.li/rsc-advances

1. Introduction

Worldwide efforts to promote the use of new energy vehicles have been significantly accelerated by the rapid development of the automotive industry and growing concerns about pollution and the depletion of fossil fuels. Electric vehicles and hybrid electric vehicles rely on rechargeable lithium-ion batteries, which are the most popular and dependable power storage technology. Their small size, safety profile, low self-discharge rate, extended cycle life, high energy density, higher operating voltage, short working time, and minimal environmental impact make them ideal for renewable energy storage. The crucial role of lithium in battery manufacturing has consequently led to its demand expanding at an exponential rate worldwide. Seawater, minerals containing lithium, brines from salt lakes, and used lithium-ion batteries are some of the many places you can find lithium.[1–3] Nevertheless, there is an urgent need for effective methods to extract lithium from primary and secondary sources, given the severe shortage resulting from increasing demand for the metal.[4]

While used batteries typically contain around 5% lithium by weight in their cathode components, the majority of that lithium originates from liquid sources, such as salt lake brines and seawater, accounting for over 60% of the total.[5] There are numerous obstacles to developing mineral deposits that contain lithium, including high costs, intense energy demands, and significant environmental implications. Thus, the most practical and long-term solution for the lithium sector is being considered as extracting from liquid sources.[6] Evaporation crystallization, electrodialysis, solvent extraction, membrane separation, nano-filtration, co-precipitation, and adsorption are some of the extraction methods that studies have investigated in an effort to overcome this difficulty.[7–11] Although there are technologies that can be used to handle low-concentration lithium in salt water and brine, lots of them have major limitations, such as requiring a lot of energy, using solvents, or not being very efficient. Among these techniques, adsorption stands out as a viable and workable option for lithium extraction from water. Among its many advantages are its ease of use, minimal energy consumption, low

[a]*Chemistry Department, College of Science, Imam Mohammad Ibn Saud Islamic University (IMSIU), Riyadh 11623, Saudi Arabia. E-mail: miissa@imamu.edu.sa*
[b]*Nuclear Materials Authority, P.O. Box 530, El-Maadi, Cairo 11728, Egypt*
[c]*Chemistry Department, Faculty of Science, Capital University (formerly Helwan University), 11795 Helwan, Cairo, Egypt. E-mail: taha1m@yahoo.com*
[d]*Chemistry Department, Faculty of Women for Art, Science, and Education, Ain Shams University, Heliopolis, Cairo 11757, Egypt*

cost, reusability, and continued efficacy at low lithium concentrations.[12] The aforementioned characteristics render adsorption highly desirable for applications involving the large-scale extraction of lithium.[13] The adsorption capability, operational effectiveness, ease of separation, regenerative potential, and total cost of the adsorption substances used are critical factors in determining the method's efficacy.[14]

The development of new lithium recovery methods has become more urgent due to the increasing global demand for lithium. This demand is anticipated to triple from 2018 levels, reaching roughly 95 000 tons by 2025.[15] Beyond its use in batteries, lithium has strategic importance in fields such as aeronautical engineering, medicine, polymer synthesis, and high-performance lubricants.[16]

Beyond simple capacity values, the design of adsorbent architecture plays a decisive role in practical lithium recovery. Carbon-based sorbents bearing carboxyl, amide, or imidazole groups have been reported to capture Li^+ from brines and battery leachates, yet they often suffer from limited site density, poor separation from slurry, or rapid loss of performance in highly saline and multi-component media. In contrast, the CNT–AMP composite developed in this work combines a mesoporous magnetic CNT backbone with a high loading of aminomethylenephosphonate groups, providing a dense array of hard oxygen donor sites and facile magnetic separation after adsorption. This structure is particularly suited for treating concentrated LIB leachates, where high ionic strength and competing cations demand both strong Li^+ binding and efficient solid–liquid separation.[17–19]

Conventional industrial routes for lithium extraction, such as solar evaporation, solvent extraction, and membrane separation, still face important challenges, including long residence times, large land and water footprints, intensive energy consumption, and the use of organic solvents, as well as scaling and fouling when treating real brines. Recent studies have therefore explored greener, adsorption-based processes for lithium recovery from complex aqueous streams, highlighting the need for sorbents that combine high selectivity, fast regeneration, and low environmental impact (*e.g.*, recent advances in lithium–selective organic–inorganic hybrids and ion-sieve architectures reported). Within this context, CNT–AMP is proposed as a sustainable, water-based adsorption system that can be coupled with hydrometallurgical battery-recycling flowsheets to selectively capture and upgrade lithium from spent LIBs.[20–22]

Several lithium-specific adsorbent materials have been created as a result. These include cellulose-acetate membranes doped with $Li_4Mn_5O_{12}$,[23] tin(IV) antimonite,[24] titanium-based lithium-ion screens,[25] manganese-based screens,[26] lithium-aluminum layers double hydroxides,[27] and titanium-intercalated lithium manganese oxides.[28] Nanocomposites imprinted with ions,[29] hybrid aerogels based on graphene,[30] and ion sieves made of manganese oxide doped with aluminum[31] are a few more famous patterns.

Recent advancements in green chemistry have further highlighted the importance of interfacial engineering and dipole modulation to enhance the selectivity and sustainability of lithium recovery from spent batteries.[32,33] Moreover, the integration of material recovery with process optimization remains a critical step towards fully circular battery economies.[34]

One of the most fascinating carbon-based nanomaterials, carbon nanotubes (CNTs), has a mesoporous architecture, a high surface area, remarkable chemical stability, and a unique tubular shape. Because of these characteristics, CNTs outperform more traditional adsorbents, such as activated carbon or clay, in terms of physicochemical durability, selectivity, and adsorption efficiency.[35] Clean CNTs, on the other hand, have problems such as being hydrophobic, experiencing difficulty recovering from water, and being vulnerable to fouling.[36] Their hydrophilicity, dispersion, and affinity for target ions have been enhanced through surface modification and functionalization techniques, which have helped to overcome these constraints.[37] Functionalized carbon nanotubes (CNTs) hold immense promise as adsorbents for a wide range of organic and inorganic pollutants, especially when it comes to processes like hydrogen bonding, π–π stacking, and interactions caused by van der Waals.[38] Studies have shown that nitric acid oxidation enhances the surface functionality of CNTs, resulting in improved adsorption efficiency for heavy metal removal, such as lead.[39,40] One study found that CNTs treated with carboxyl and group hydroxyl greatly enhanced the efficacy of Pb(II) adsorption.[41]

This study's overarching objective is to develop and manufacture an innovative functionalized carbon nanotube-based adsorbent specifically engineered to remove lithium ions from water, with a focus on spent lithium-ion battery leachates. We will confirm the structure and surface chemistry of the produced material by conducting detailed characterization. To find the best operating parameters, we will run batch adsorption experiments with different pH, contact time, starting ion concentration, and doses of adsorbent. In addition, the adsorption mechanism will be better understood by applying kinetic and thermodynamic simulations. The overarching goal of this study is to assess the recovery and purity of lithium and related precious metals like cobalt from battery trash to provide an efficient and environmentally friendly method for recycling lithium.

2. Experimental

2.1. Materials and apparatus

Materials obtained from the Shanghai Chemical Reagent Company, including $FeCl_3 \cdot 6H_2O$, ethylene glycol, ethanol, 1,6-hexanediamine, and CH_3COONa. Sigma-Aldrich in Missouri, USA, is where it gets phosphorus oxychloride ($POCl_3$) (99%), 4-hydroxy-2-butanone (99%), thionyl chloride, aluminum chloride, and dimethylformamide (DMF). The Egyptian Petroleum Research Institute (EPRI) supplied the carbon nanotubes. Every chemical that was employed was an analytical grade and was applied exactly as received, without any further refinement. Merck Chemical Company was contacted to get lithium chloride. The de-ionized water used in all the working solutions had a pH range of 6 to 7, and the purity level was 18.2 MΩ cm.

2.2. Salt solution formulation

Using a volumetric flask, 1.0 g of LiCl was submerged in Milli Q water to generate a 1000 ppm LiCl solution. The final

volume was then adjusted to 1 liter. In a similar vein, a 0.1 M LiCl mixture was prepared by dissolving 4.24 g of LiCl in Milli Q water and then adding 1 liter of water using a volumetric flask.

2.3. Formulation of amine-functionalized magnetite nanoparticles

Synthesis of amine-functionalized magnetite nanoparticles (AM) was accomplished by modifying an already described

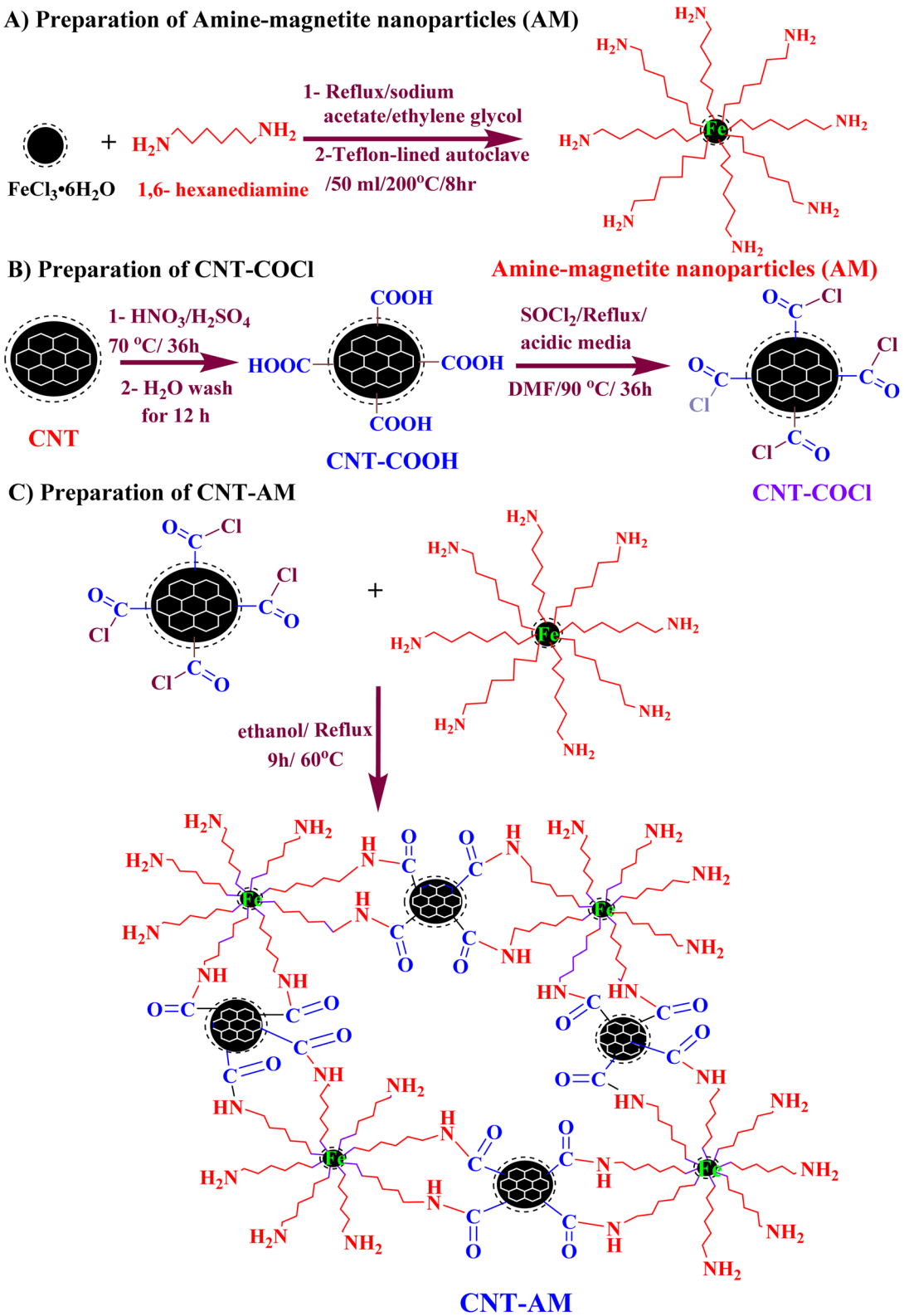

Fig. 1 Schematic representation of the stepwise preparation of CNT–AM.

flexible solvothermal process (Fig. 1A).[42] The standard procedure involves adding 1.0 g of $FeCl_3 \cdot 6H_2O$, 6.0 g of 1,6-hexanediamine, and 2.0 g of anhydrous sodium acetate to 40 mL of ethylene glycol and then vigorously agitating the mixture to form a translucent solution. After that, 50 mL of this mixture was placed in a Teflon-lined autoclave and subjected to high heat (200 °C) for 8 hours. The product was collected using a magnet, rinsed with deionized water, and finally dried under vacuum.

2.4. Oxidation of carbon nanotubes

The oxidation of carbon nanotubes (CNTs) to incorporate carboxylic acid (–COOH) groups (Fig. 1B) is a fundamental technique used to enhance their solubility and facilitate further chemical modification. First, 5 g of carbon nanotubes (CNT) were combined with 0.5 L of a 1 : 3 vol solution of sulfuric acid and nitric acid in a round-bottom flask. The mixture was stirred and subjected to 70 °C with a reflux condenser for a minimum of 36 hours to organize carboxyl functional compounds on the nanotubes, and so CNT–COOH is formed. To extract the powder product, the sample was cooled to ambient temperature and subsequently centrifuged.[43,44] Before using it, the collected powder was repeatedly rinsed with deionized water until the filtrate pH was close to a neutral pH (~7). Then, the final product was oven-dried at 100 °C for approximately 12 hours. The chlorination reaction (Fig. 1B), which involved coming CNT–COOH into contact with the $SOCl_2$ solution, replaced any hydroxyl groups with chloride in the final powder product (CNT–COCl). The mixture was heated to 90 °C and maintained at this temperature in DMF under continuous stirring for 36 h to ensure complete reaction (conditions denoted as DMF/90 °C/36 h in Fig. 1B).

2.5. Preparation of amine-functionalized magnetite carbon nanotubes (CNT–AMP)

An amine-functionalized magnetite nanoparticle (AM) suspension in an ethanolic solution of 50 mL was subjected to 30 minutes of ultrasonication. It followed the dispersion of 3 grams of chlorinated CNTs in 300 milliliters of ethanol, followed by the addition of the ultrasonicated nanoparticles (Fig. 1C). After refluxing for 9 hours at 60 °C, the liquid was cooled. The functionalized CNTs were then collected by centrifugation. Before being used, the amine-functionalized magnetite at CNTs (CNT–AM) sample was rinsed multiple times with deionized water and then oven-dried at 60 °C for approximately 5 hours.

2.6. Preparation of amine-functionalized magnetite phosphonate derivatives of CNTs (CNT–AMP)

The synthesis of the intermediate hydroxybutanone-functionalized composite (CNT–AHB) (Fig. 2) was performed *via* a condensation reaction in a 250 mL triple-neck round-bottom flask equipped with a reflux condenser and a mechanical stirrer. In this step, 3.0 g of the previously prepared CNT–AM was dispersed in 75 mL of DMF and treated with 6.69 g (5.0 mmol) of 4-hydroxy-2-butanone. The mixture was heated to 90 °C and maintained at this temperature under continuous stirring for 36 h to ensure complete reaction (conditions denoted as DMF/90 °C/36 h in Fig. 2). Upon completion, the solvent was removed using a rotary evaporator, yielding the solid CNT–AHB intermediate, which was then subjected to phosphorylation to synthesize CNT–AMP as described below.

The final step was to reflux 1 g of CNT–AHB and 0.15 g of anhydrous $AlCl_3$ with 20 mL of $POCl_3$ in DMF. This was performed for 24 hours at 100 °C as illustrated in Fig. 2, with a tail gas absorber to absorb any HCl that may have leaked during the process. After that, the mixture was slowly cooled for a few minutes in an ice bath and then given 200 mL of distilled water. The final product, CNT–AMP, was subjected to multiple washes with pure C_2H_5OH before being dried at 80 °C for 12 hours.

2.7. Characterization of materials

In this work, various analytical approaches were employed to evaluate the properties and efficacy of the manufactured CNT–AMP material for lithium adsorption. The pH level was measured using a Digimed DM-21 computerized pH meter, which has a precision of ±0.1. With the help of a Vibromatic-384 shaking device, an exact amount of a solution comprising lithium was combined with an exact weight of CNT–AMP material for the balance tests. Inductively coupled plasma emission spectroscopy (ICP-OES, PerkinElmer Inc Avio 220) was used to determine the amounts of Li^+, Na^+, K^+, Mg^{2+}, and Ca^{2+} ions in the solution.

An FT-IR 4100 Gasco-Japan analyzer equipped with KBr disks was used to record the infrared (IR) spectra. Examination employing X-ray Photoelectron Spectroscopy (XPS) was carried out using a Kratos Axis Ultra spectrometer (Manchester, UK) that had a 225 W monochromatic Al K_α X-ray source. After degassing the material at 100 °C under vacuum, the CNT–AMP material was subjected to Brunauer–Emmett–Teller (BET) examination (ASAP-2460) to ascertain its surface area and pore size variability. A vibrating sample magnetometer (VSM; Model Quantum Design, PPMS-14) was used to conduct magnetization measurements at room temperature. A high-resolution transmission electron microscope (HR-TEM, model JEOL-JEM 2100, Japan) was used for examining the surface morphologies of the set-up composites. The increasing voltage was set at 200 kV.

Spectroscopic examination was carried out at 293 K on solutions dissolved in DMSO solvent, and Nuclear Magnetic Resonance (NMR) spectroscopy (^1H and ^{13}C) was obtained using a Bruker Mercury 400 analyzer set at 400 MHz. Chemical shifts (δ) are given in parts per million (ppm), while binding constants (J) are provided in Hertz (Hz).

The Bruker Autoflex Speed MALDI-TOF mass spectrometer (Germany) was used for the MALDI-TOF-MS analyses. The instrument had a nitrogen laser that emitted light at 337 nm and could operate within an accelerating potential range of +20/−20 kV. Carbon nanotubes containing the analyte were deposited and dried on a ground-steel target to prepare specimens for laser irradiation. With careful optimization, the laser energy was reduced to a level just over the ionization threshold, allowing for better resolution and signal-to-noise ratios. All

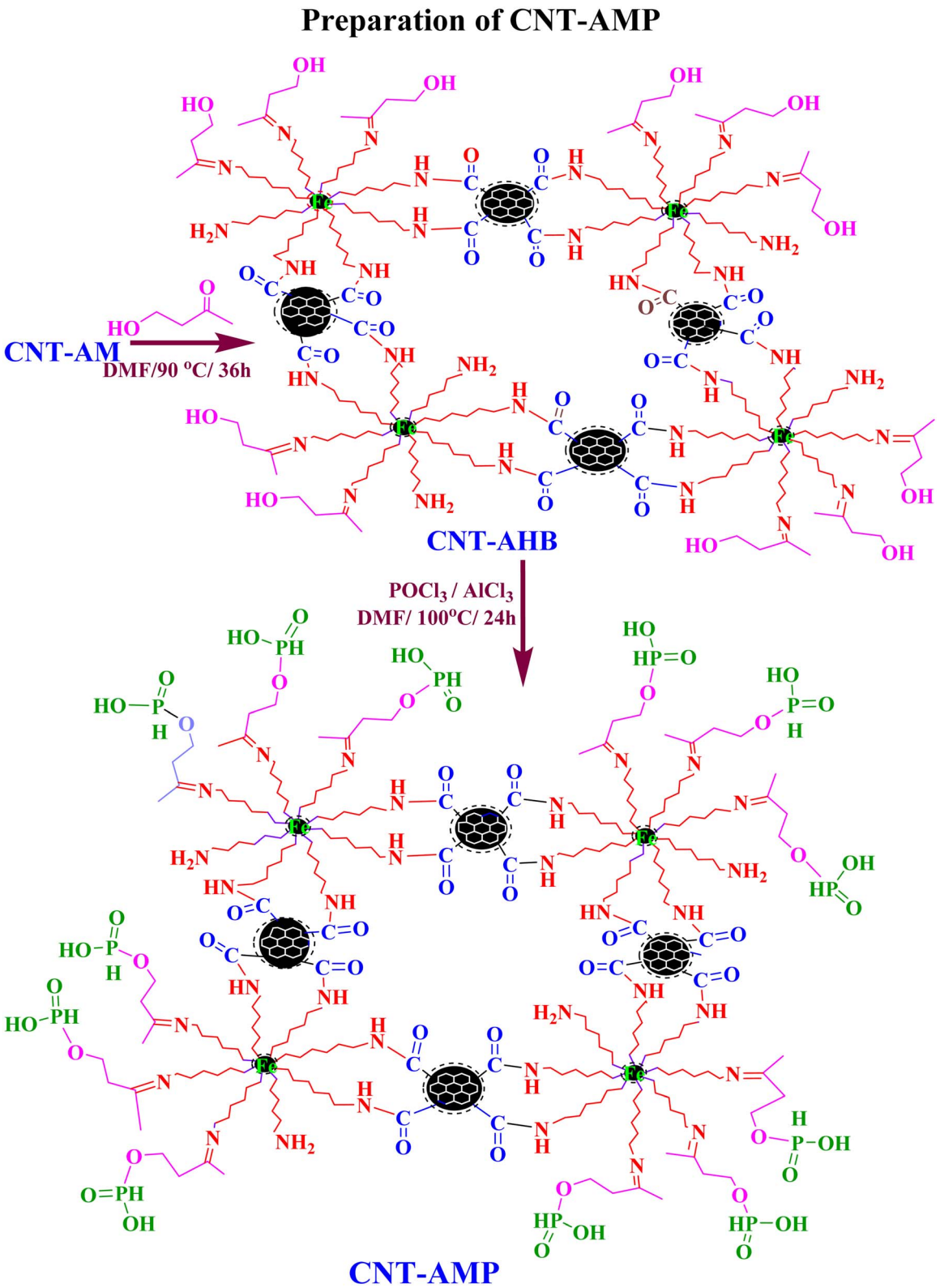

Fig. 2 Schematic representation of the stepwise preparation of CNT–AMP.

mass spectra, unless stated differently, were collected using positive-ion reflection mode in a high vacuum (pressure < 1×10^{-4} Pa) with a 40 ns delay in extraction; each spectrum is an average of 30 laser pulses. To provide precise mass assignment and trustworthy data interpretation, a calibration with a point standard that encompasses the mass range of interest was rigorously used for external mass calibration.

The X-ray diffraction (XRD) method was developed in the Netherlands, utilizing an X-ray machine model PW-3710 with a PW-1830 generator. A Cu-target tube running at 40 kV and 30 mA with a Ni filter was utilized for X-ray radiation. To conduct the ESEM investigations, the Environmental Scanning Electron Microscope (ESEM, Version EXL 30, Netherlands) was used.

2.8. Adsorption experiment of CNT–AMP

An aqueous solution of Li(I) was used as the basis for an indicative adsorption test, with the adsorption material CNT–AMP added at a specific solid–liquid ratio. The mixture was heated in a thermostatic water bath before passing through a 0.45 μm membrane filter, which allowed the quantities of metal ions in the filtrated solution to be assessed by ICP-OES. The assessment of adsorption achievement was established using eqn (1)–(3).

$$q_e = (C_0 - C_e) \times \frac{V}{m} \quad (1)$$

$$E\ (\%) = \left(\frac{C_0 - C_e}{C_0}\right) \times 100 \quad (2)$$

$$K_d = \left(\frac{C_0 - C_e}{C_e}\right) \times \frac{V}{m} \quad (3)$$

The rate of adsorption at balance is represented by q_e (mg g^{-1}), and the efficiency of adsorption is represented by E (%). The distribution coefficient (K_d) of metal ions concerning Li(I) can be calculated using eqn (3). Li(I) initial and equilibrium concentrations are denoted by C_0 and C_e, respectively, in milligrams per liter; the volume of the aqueous phase is represented by V, in milliliters; the mass of the dry adsorbent is represented by m, in grams.

Solutions of Li(I) in the pH intervals 1–12 were generated for the pH-dependent studies of CNT–AMP towards Li(I). Li(I) solutions were adjusted to certain pH values using HCl or NaOH solutions. The starting concentrations of the solutions were 250 mg L^{-1}. Equal amounts of Na(I), K(I), Ca(II), and Mg(II) were used in the adsorption selectivity tests, which ranged from 50 to 250 mg L^{-1}.

2.9. Desorption experiments

After removing any impurities with deionized water, 3 g of CNT–AMP adsorbent was mixed with 20 mL of desorbing solution and placed in a beaker. The beaker was then placed in a water bath maintained at a constant temperature of 25 °C for various durations. The concentration of metal ions in the desorption solution was measured using ICP-OES. The desorption efficiency (DE, %) was determined using eqn (4).

$$\mathrm{DE}\ (\%) = \frac{C \times V}{q \times m} \quad (4)$$

In this context, C represents the metal ion concentration in the solution (in mg L^{-1}), V stands for the volume of the desorbed solution (in mL), m for the mass of the CNT–AMP adsorbent (in g), and q for the capacity of the adsorbent to adsorb metal ions (in mg g^{-1}).

3. Results and discussions

3.1. Characterization of materials

3.1.1. FTIR inspection of oxidized CNT, CNT–AM, and CNT–AMP. The vibratory stretching peak of the functional group hydroxyl (–OH) in Fig. 3 could be the reason for the wide band at 1622–1625 cm^{-1} and a powerful peak focused at 3435–3443 cm^{-1} in certain oxidized CNTs.[45] The C–H bonds in alkanes induce anti-symmetric and systematic tension vibrations, which are represented by the tiny maxima around 2918 cm^{-1} and 2850 cm^{-1}.[46] The vibrations caused by stretching of the carbonyl and carboxyl groups were associated with the usual maxima at 1722 and 1390 cm^{-1}.[47] The C–O stretching vibration and the –OH bending vibration of the alcohol and phenol units could be the reason for the wide peak at 1098–1113 cm^{-1}.[48]

The FTIR results revealed that in the case of CNT–AM, the –OH quantity of the FeO_x@CNTs rose at 3451 cm^{-1} and 1622 cm^{-1}, while the carboxyl peak at 1390 cm^{-1} decreased or even disappeared. This suggests that the carbonyl groups are responsible for the –OH and carboxyl heights at 1719 cm^{-1} as they interact with the amine-functionalized nanocomposite. It is confirmed that the free 1,6-hexadiamine was successfully bound to the surface of carboxylated CNTs since the absorption peaks near 3382 cm^{-1} correspond to the typical absorption of the N–H stretching vibration of the compound. The presence of C=N stretching groups can be explained by the peaks seen at 1612 cm^{-1}.

The chemical changes brought about by the process are highlighted by the emergence of new absorption bands located at 2356 cm^{-1}, 1174 cm^{-1}, and 993 cm^{-1}, respectively, after phosphorylation (Fig. 3). These bands indicate the creation of P–H, P=O, and P–OH stretching vibrations.[49] The phosphonate groups were successfully introduced, and the hydroxyl group peaks disappeared, confirming agreement.

3.1.2. XPS analysis of CNT–AMP. Examining a material's elemental makeup, chemistry states, and bonding settings is possible with the use of XPS, a potent surface examination method. Before and after lithium adsorption, the surface composition of CNT–AMP is compared in the supplied XPS spectra (Fig. 4).

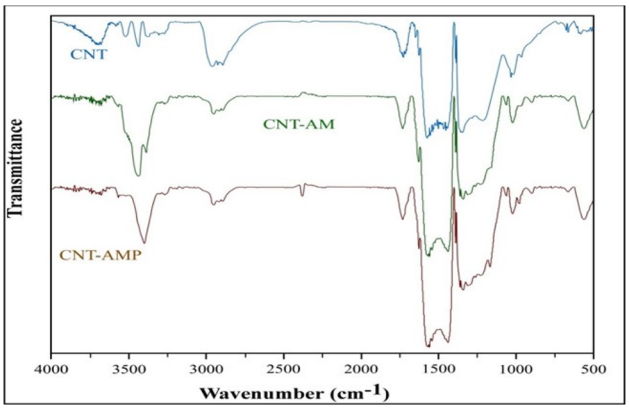

Fig. 3 FTIR analysis of CNT, CNT–AM, and CNT–AMP adsorbent.

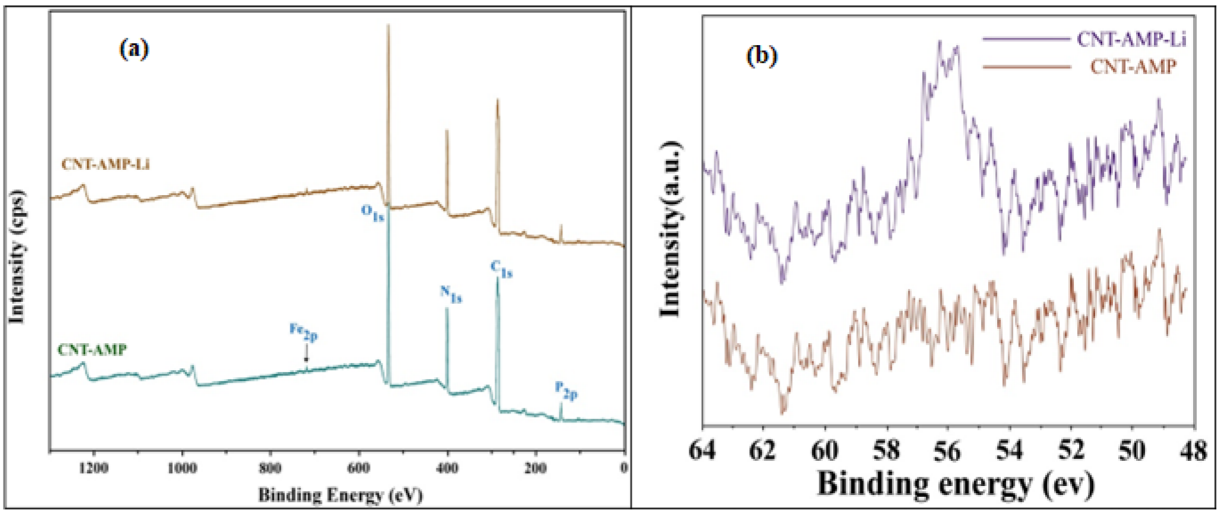

Fig. 4 (a) XPS survey spectra and core-level analysis of CNT–AMP before and after Li^+ adsorption. (b) Plot of the Li 1 s region (64–48 eV) compares pristine CNT–AMP and Li-CNT–AMP, showing the absence of a Li 1s feature in the fresh material and the appearance of a distinct Li 1s peak at ≈55–56 eV after adsorption.

3.1.2.1. Elemental composition and identification. Different parts of the CNT–AMP structure are represented by distinct spectra peaks (Fig. 4a): O 1s (~530 eV) reflects the oxygen-containing functional groups (hydroxyl and phosphate-related bonds) stated during AMP functionalization, N 1s (~400 eV) represents the carbon framework, which mainly comes from the CNT–AMP, and C 1s (~285 eV) represents the carbon nanotube framework. Fe 2p (~710 eV, faint peak)[50] implies trace iron contamination or the potential existence of leftover catalyst from CNT production, while P 2p (~133 eV) shows the existence of phosphonate ($-PO_2H_2$) groups from the AMP moiety, which are essential for metal ion adsorption.

3.1.2.2. Lithium adsorption and spectral changes. The following alterations are noticeable after lithium adsorption (Fig. 4): the presence of a newly formed Li 1s peak (~54–56 eV) in Fig. 4b indicates that lithium has been successfully adsorbed onto CNT–AMP. Multiple functional groups (such as phosphate or oxygen groups) may interact, as indicated by the broad peak. The intensities of the phosphorus and oxygen peaks show a modest shift and/or modification, suggesting that Li^+ ions may be coordinated with phosphonate ($-PO_2H_2$) groups. So, it's clear that the AMP group helps in lithium binding. If the N 1s peak shifts or changes in intensity, it could be because lithium interacts with amine ($-NH_2$) or imine (–C═N) functional groups, which can lead to adsorption. The steadiness of the C 1s peak over time suggests that the carbon nanotube (CNT) backbone is not directly involved in lithium binding but rather acts as a scaffold for the functional groups, since it shows limited variation.

To visualize the lithium signal more clearly, the Li 1 s binding-energy region was isolated and plotted for both pristine CNT–AMP and Li-loaded CNT–AMP over the 64–48 eV range (Fig. 4b). In the pristine material (CNT–AMP), this region shows only low-intensity background fluctuations and no distinct feature at 54–56 eV, indicating the absence of surface lithium. After exposure to Li^+ solution, the spectrum of CNT–AMP–Li displays a pronounced peak centered around 55–56 eV, which can be attributed to the Li 1s core level. The use of the same energy window and comparable intensity scaling for both spectra highlights the emergence of the Li 1s signal and provides direct spectroscopic evidence for lithium uptake on the CNT–AMP surface.

3.1.2.3. XPS analysis and mechanism of lithium adsorption. The XPS spectrum data suggest that electrostatic interactions between positively charged Li^+ ions and the negatively charged phosphonate ($-PO_2^{2-}$) groups are the most probable mechanism for lithium adsorption on CNT–AMP. An amine or imine functional group can chelate lithium at nitrogen sites, facilitating complexation. Surface groups (such as hydroxyl and carboxyl) that contain oxygen form hydrogen bonds with Li^+. The material's promise for lithium recovery from water-based

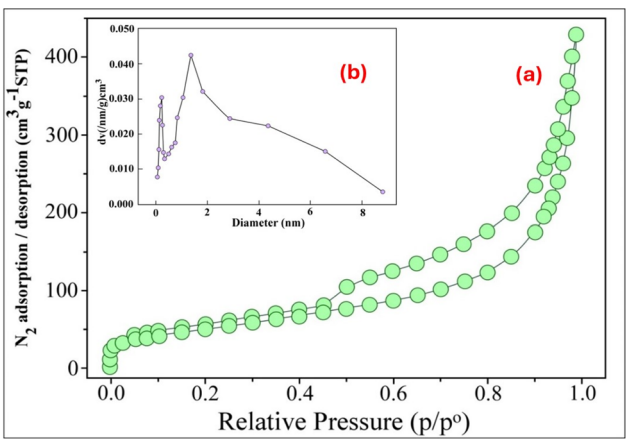

Fig. 5 (a) BET analysis of the isotherm of adsorption–desorption trend, and (b) the pore size distribution of the mesoporous nature of CNT–AMP.

systems is confirmed by the fact that these interactions cause lithium to be retained on the CNT–AMP surface.

3.1.3. BET and pore structure analysis of the CNT–AMP. Fig. 5a shows that CNT–AMP's N_2 adsorption–desorption isotherm is a type-IV isotherm with a well-defined hysteresis loop, which is indicative of a mesoporous structure. The presence of micropores is suggested by the abrupt rise in N_2 intake at relatively low pressure ($P/P_0 < 0.1$), but the steady rise at higher pressures suggests the involvement of mesopores. The CNT–AMP has a total pore volume of 0.40 $cm^3\ g^{-1}$, a mean pore diameter of 1.63 nm, and a BET surface area of 159.63 $m^2\ g^{-1}$. Fig. 5b shows the distribution of pore sizes, which provides more evidence that CNT–AMP is mesoporous. Most of the pores are nanometers in size. These findings prove that carbon nanotubes can be improved for adsorption by modifying them to increase their surface coverage and improve their pore properties.

3.1.4. Magnetic evaluation. Fig. 6 displays the results of an evaluation of the magnetic characteristics of amine-functionalized magnetite nanoparticles and CNT–AMP conducted at ambient temperature employing a vibrating sample magnetometer (VSM) with a magnetic field spanning −20 to 20 kOe. Both materials' hysteresis loops exhibited ferromagnetic characteristics. It was found that the CNT–AMP nanocomposite had a magnetic saturation value of 56.17 emu g^{-1}, while the amine-functionalized magnetite nanoparticles had a value of 72.18 emu g^{-1}. The presence of 4-hydroxy 2-butanone and phosphonate groups on the surface of the magnetite may explain why the nanocomposite's magnetic saturation is reduced. The significant magnetic responsiveness of the produced nanocomposites is demonstrated by their excellent magnetic characteristics, which enable them to be easily separated from a liquid using an external magnetic field.

3.1.5. TEM analysis of CNT–AMP. TEM images confirm the successful incorporation of aminated magnetic phosphorite (AMP) nanoparticles within the internal cavities of CNTs. The first micrograph (scale: 100 nm) in Fig. 7a shows a more complex network of CNTs, within which AMP nanoparticles are

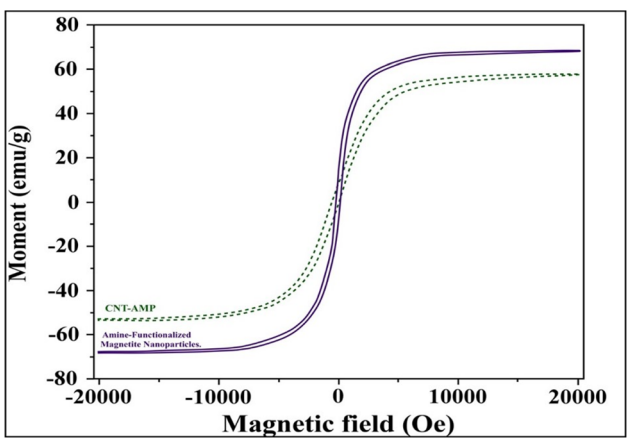

Fig. 6 Magnetization investigations of CNT–AMP and amine-functionalized magnetite nanoparticles.

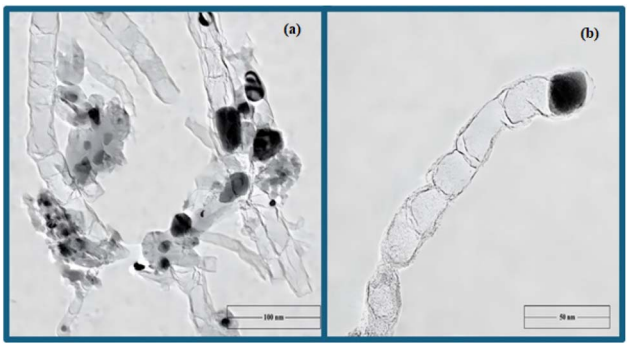

Fig. 7 TEM analysis of the CNT–AMP adsorbent, (a) scale: 100 nm, (b) scale: 50 nm.

also observed. These particles appear either as discrete units or as small aggregates, predominantly located inside the nanotubes rather than on their outer surfaces. This spatial confinement likely prevents external agglomeration and promotes the better dispersion of nanoparticles.

The second micrograph (scale: 50 nm) in Fig. 7b reveals the characteristic segmented, bamboo-like architecture of the CNTs, with clearly defined internal compartments. Within these hollow sections, dark-contrast regions indicate the presence of electron-dense AMP nanoparticles, suggesting that the nanoparticles are effectively confined inside the nanotube structure.

Overall, the TEM results validate the formation of a well-integrated CNT–AMP composite material, where the magnetic and aminated functionalities are successfully encapsulated within the nanotube matrix. This configuration is expected to improve the material's magnetic responsiveness, surface functionality, and structural stability, making it a suitable candidate for use in adsorption processes, catalytic systems, and magnetic recovery applications.

3.1.6. ^{1}H-NMR analysis. Fig. 8 shows the results of the 1H-NMR characterization of the CNT–AMP adsorbent. ^{1}H-NMR (DMSO-d_6, 25 °C, 400 MHz, TMS) δ, ppm: 11.63 (s, –COOH), 4.38 (s, –OH), 7.54 (s, –NH, $J = 4.93$ Hz), 5.31 (s, –PH, $J = 3.1$ Hz), 8.84 (s, –POOH, $J = 3.1$ Hz), 2 (s, $-CH_3$), 1.36 (m, $-CH_2$, $J = 6.38$ Hz), 2–2.79 (m, –CH, $J = 8.8$ Hz), 1.29–4.11 (m, $-CH_2$ branch). A ^{1}H-NMR study using DMSO-d_6 as a diluent and an energy of 400 MHZ provides valuable information regarding the distribution of protons in the synthesized CNT–AMP, a material that assists in the prediction of its structure. To symbolize the synthesized composite, there are primary assignments.

At 11.63, 4.38, 7.54, 5.31, and 8.84 ppm, there are noticeable assignments that represent the composite's important functional groups. These groups correspond to the remaining carboxylic acid group (a more de-shielded proton), the remaining hydroxyl group attached to the modified CNT skeleton, the amino group (–NH) of the amide engaged site, the proton of the phosphine group, and the proton of the phosphonic acid.

At 1.36 and 2.79 ppm, respectively, the methylene and methine protons were assigned to the skeleton of the modified CNTs. In addition, there is a 2 ppm chemical shift due to the methyl protons that are bound to the imine carbon, which show up as singlets.

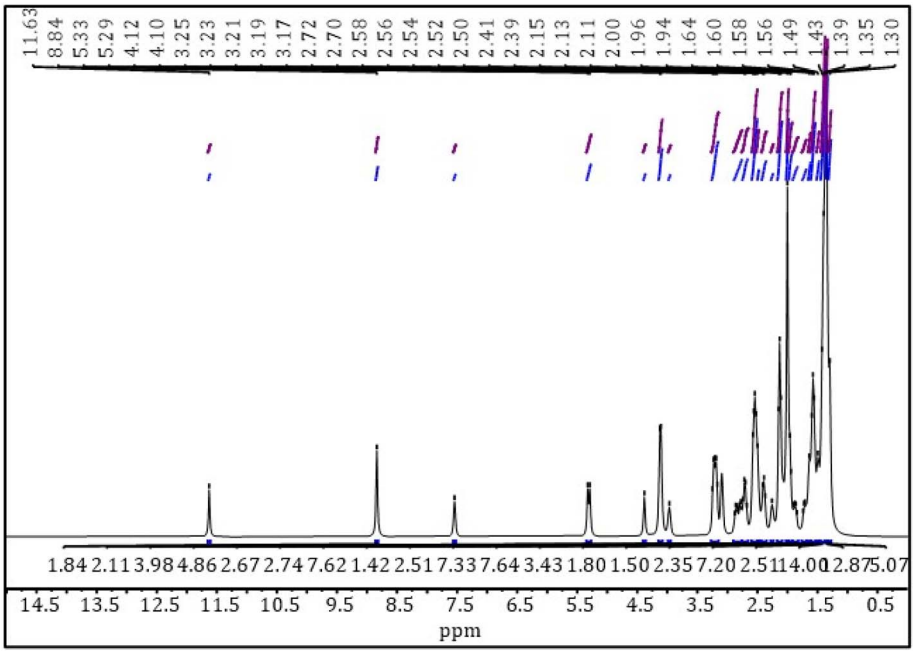

Fig. 8 ^{1}H-NMR analysis of CNT–AMP adsorbent.

Also, within 1.29 and 4.11 ppm, a chemical shift of the methylene protons in the branches containing nano-iron was noted.

3.1.7. ^{13}C-NMR analysis. The CNT–AMP adsorbent that was produced was characterized using ^{13}C-NMR, as shown in Fig. 9. ^{13}C-NMR (25 °C, DMSO-d_6, 100 MHz, TMS) δ, ppm: 181.32 (s, –COOH), 176.33 (s, –CO–NH_2), 166.55 (s, –N=C–CH_3), 22.46 (s, –N=C–CH_3), 28.89–34.96 (s, –CH_2 of modified CNTs), 33.41–45.7 (s, –CH of modified CNTs), 46.51 (s, –CH–COOH), 73.25 (s, –CH–OH), 26.14–62.91 (s, –CH_2 branch). A useful instrument that provides considerable data about the carbon atoms in the produced CNT–AMP adsorbent is ^{13}C-NMR analysis with an energy of 100 MHz and DMSO-d_6 as a diluent. The synthesized composite clearly demonstrates the presence of the carbon skeleton, one of the primary assignments.

There are a few carbon assignments that indicate important carbon contents in the composite. These include the carbon atoms linked to the amide group, the carbon atoms at the active site of the imine group, the carbon atoms attached to the carboxylic acid (more de-shielded carbon), and the carbon atoms at 181.32, 176.33, and 22.46 ppm, respectively. At 28.89–34.96, 33.41–45.7, 46.51, and 73.25 ppm, there are numerous significant assignments to methylene, methine, methine carbon connected to the carboxylic acid group, and methine carbon linked to the hydroxyl group that make up the skeleton of modified CNTs. Also, a chemical change of 26.14 to

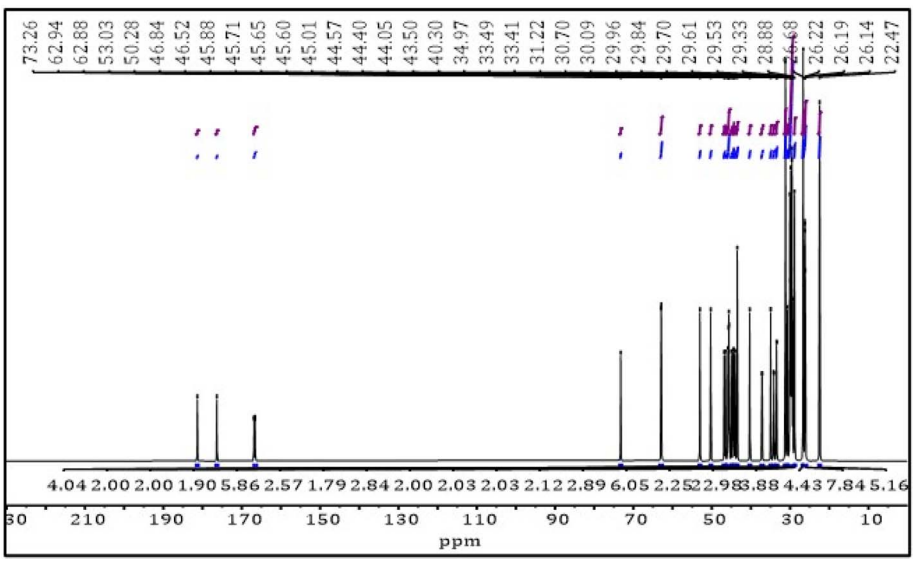

Fig. 9 ^{13}C-NMR analysis of CNT–AMP adsorbent.

62.91 ppm was seen in the methylene carbon of the branching that contained nano-iron.

3.1.8. Mass spectrometric assessment. The mass spectra of the CNT–AMP adsorbent are shown in Fig. 10. The MALDI-TOF/MS results show the qualified abundances of the following chemical shifts: 552, 417, 240, 234, 206, 150, 86, 81, 69, 65, 64, 57, 56, 54, 52, 50, 45, 44, 29, 28, 26, 18, 17, 15, and 14. Regarded as a potent analytical tool for mass spectrometry (MS) examination of modified carbon nanotubes (CNTs) and other large molecular weight composites, matrix-assisted laser desorption/ionization time-of-flight (MALDI-TOF) is compatible with high-throughput analysis *via* a fragmentation pattern and has excellent sensitivity and resolution.[51]

Several significant patterns of fragmentation were discovered, all of which are linked to the recently produced modified CNs. There are two primary components to these designs; one deals with the nano-iron branch, and the other is relevant to the CNTs moiety. Observations for the nano-iron branch included fragments of $[C_{22}H_{46}FeN_2O_6P_2]$ with an approximate abundance of 34%, $[C_{17}H_{34}FeN_2O_4P]$ with an in-relation abundance of 13%, $[C_{11}H_{22}FeNO]$ with an in-relationship abundance of 11%, and $[C_{10}H_{21}FeNO_3P]$ with a relative abundance of 58%. Pay close attention to the mass spectra of nano-iron; three iron isotopes were detected at $m/z = 54$, $m/z = 56$, and $m/z = 57$, with corresponding average abundances of 6%, 92%, and 2%, respectively, guaranteeing the successful incorporation of nano-iron into the composite.[52] Moreover, other fragments serve as markers for the composite's effective phosphonation and amidation, such as the $[H_2O_2P]$ fragment ($m/z = 65$, 13% compared abundance), the $[H_2O_3P]$ fragment ($m/z = 81$, 27% compared abundance), the $[C_4H_9NO_3P]$ fragment ($m/z = 150$, 15% compared abundance), the $[C_8H_{17}NO_3P]$ fragment ($m/z = 206$, 15% compared abundance), and $[NH_3]$ ($m/z = 17$, 10% compared abundance). In addition, numerous fragments, including $[C^+]$ or $[C^{2+}]$ with $m/z = 12$ and an approximate abundance of 93%, $[CH_3^+]$ with $m/z = 15$ and a compared abundance of 27%, $[C_2H_4^+]$ or $[CO^+]$ with $m/z = 28$ and a compared abundance of 19%, $[C_4H_4^+]$ with $m/z = 52$ and a compared abundance of 33%, $[CO_2^+]$ with $m/z = 44$ and a compared abundance of 16%, $[H_2O^+]$ with $m/z = 18$ and a compared abundance of 53%, and $[COOH^+]$ with $m/z = 45$ and a compared abundance of 29%.[53] It is clear from the available data that the various functionalization techniques used to create the CNT–AMP adsorbent were effective.

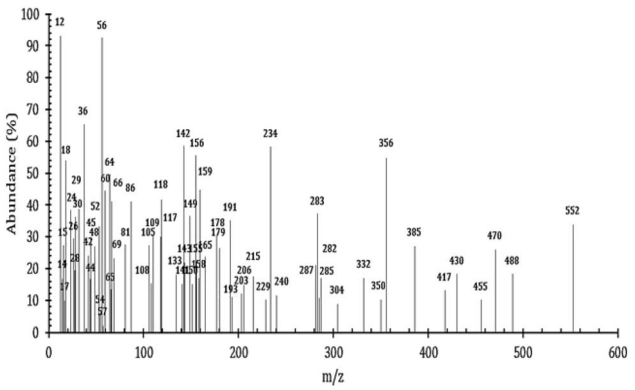

Fig. 10 Mass spectra assessment of CNT–AMP adsorbent.

3.2. pH impact of Li^+ adsorption on the CNT–AMP

Lithium ions speciation and electrostatic potential are both affected by the solution pH, which in turn affects the adsorption behavior of these ions. The adsorption efficiency of CNT–AMP shows a clear rising trend from 2.0 to 12.0 pH, as shown in Fig. 11a, peaking at 226.75 mg g^{-1} at pH 12. Extensive protonation of oxygen-containing functional groups on the CNT–AMP surface occurs at pH levels below three due to the presence of hydrogen ions.[54] The capacity of oxygen atoms to donate electrons is reduced due to this increased protonation, leading to electrostatic repulsion against Li^+ ions that approach. The concentration of hydrogen ions decreases with increasing pH, allowing surface functionalities to be deprotonated gradually. This change enhances the material's ability to attract Li ions, as it fosters more favorable electrostatic interactions. Isoelectric point (pH_{IEP}) behavior closely matches the steady growth in adsorption capacity with pH increasing from 3.0 to 12.0. At a pH of 12, adsorption is most effective. However, currently, the absorption of lithium begins to drop. In extremely acidic environments, Li^+ ions tend to combine with OH^- ions, creating bigger coordination species. These species are unable to pass through the CNT–AMP structure's pores or binding sites, which decreases the efficacy of adsorption.[55]

The adsorbent shows improved selectivity for Li^+ at pH 12, as well as a significant increase in adsorption capacity, reaching 226.75 mg g^{-1} without sacrificing selectivity, as demonstrated in Fig. 11b, which is a comparison of selectivity at pH seven and pH 12. Based on batch equilibrium measurements and a plot of starting *versus* final pH values (Fig. 11b), it is observed that CNT–AMP has an isoelectric point (pH_{IEP}) of 6.8. This is the pH at which the net surface charge of the CNT–AMP becomes neutral. The surface gains a net negative charge at pH levels greater than 6.8, which enhances the electrostatic attraction of cationic ions like Li^+. Therefore, under these circumstances, Li^+ adsorption is preferable. At a pH lower than this, on the other hand, the surface becomes positively charged, which results in less adsorption. The major adsorption mechanism is controlled by the electrostatic interaction with the negatively charged CNT–AMP and Li^+ ions, so this parameter is crucial for metal ion sorption.

3.3. Effect of CNT–AMP dose on Li^+ removal

The effect of different CNT–AMP adsorbent doses on the adsorption effectiveness was carefully examined once the ideal pH settings for Li^+ capture were determined. Finding the right amount of adsorbent is essential for cutting down on material usage and operational costs. With an increase in adsorbent dose from 0.02 g to 0.08 g, the effectiveness of the adsorption of Li^+ ions showed a significant improvement, going from 27.4% to 78.6%, as shown in Fig. 12.

Beyond 0.108 g, however, increasing the amount of adsorbent did not further improve the removal effectiveness. Higher adsorbent dosages improve overall adsorption performance because

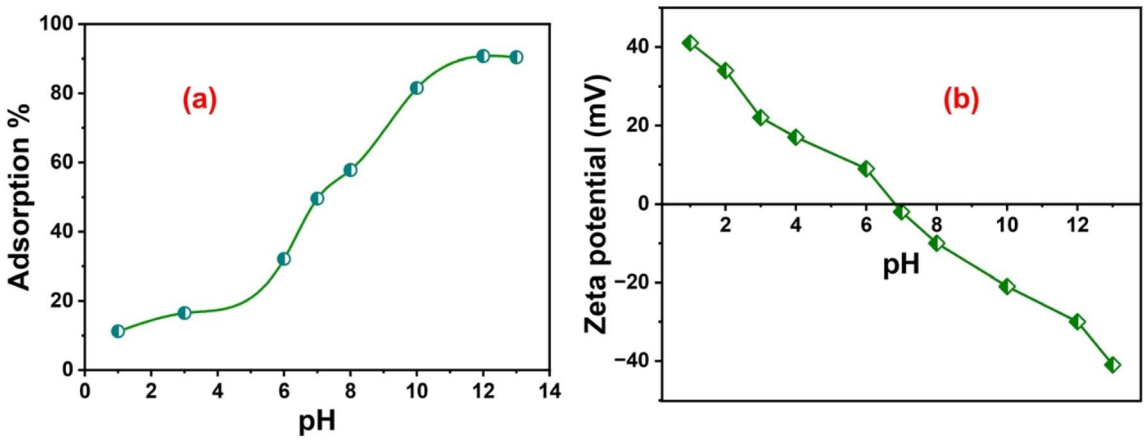

Fig. 11 (a) pH consequence of Li^+ adsorption using CNT–AMP adsorbent, (b) pH_{IEP} of the CNT–AMP adsorbent (250 mg L^{-1} Li^+, 0.1 g CNT–AMP, 90 min, 30 °C).

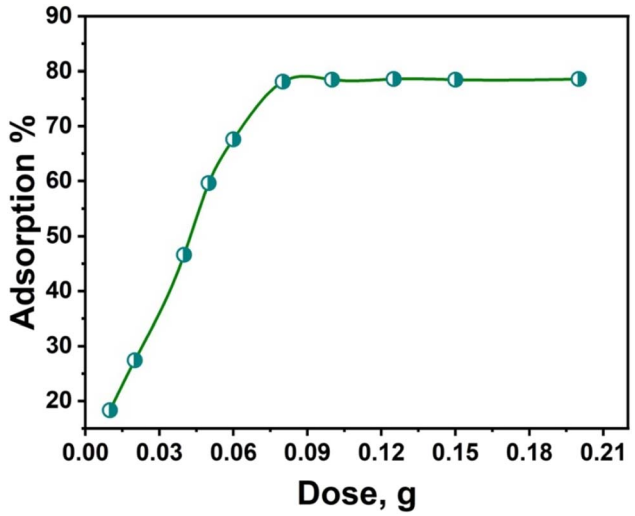

Fig. 12 The influence of a CNT–AMP dose on Li^+ adsorption process by CNT–AMP.

there are more active binding sites available, increasing the probability of ion-adsorbent interactions. This behavior is a result of this effect. The removal efficiency reaches a plateau after the adsorbent surface becomes saturated with lithium ions; increasing the adsorbent mass further does not enhance absorption. According to the results, the system reaches equilibrium with little improvement after dosing 0.08 g, which reflects an environment where Li ions effectively occupy the surface sites of CNT–AMP, thereby maximizing their adsorption effectiveness.[56]

3.4. Influence of adsorption time

The efficacy of adsorption rules is heavily influenced by the time needed to reach adsorption balance. To analyze this, a battery of batch tests was conducted to determine how ideal circumstances (adsorbent dose = 0.08 g, pH = 12, temperature = 298 K, and initial concentration = 600 mg L^{-1}) affected the adsorption of Li^+ ions as a function of contact time. The results of this study are shown in Fig. 13a. Because there were so many active binding sites available at the start of the process and the solution-to-adsorbent surface concentration gradient was so high, the adsorption capacity increased rapidly in the first 120 minutes.[57] The adsorption capacity leveled out after 120 minutes, indicating that equilibrium had been achieved. Hence, under these conditions, the ideal contact time for CNT–AMP to achieve maximum Li^+ absorption was determined to be 120 minutes.

The kinetic parameters and the adsorption mechanism were better understood with the use of linear fitting techniques. The pseudo-first-order (PFO) system (eqn (5), Table 1), the pseudo-second-order (PSO) type (eqn (6), Table 1), the Elovich type (eqn (7), Table 1), and the intra-particle diffusion (IPD) simulation (eqn (8), Table 1) were some of the regularly used kinetic models that were used to analyze the experimental data. The complete kinetic activity of lithium binding onto the CNT–AMP layer was evaluated using this multimodal approach. The kinetic modeling of PFOs is defined by the following equation:[58]

$$\log(q_e - q_t) = \log q_e - \frac{K_1 t}{2.303} \quad (5)$$

The quantity of Li^+ trapped on the adsorbent at balance and time t is represented by q_e and q_t, respectively, in mg g^{-1}. A PFO kinetic rate constant, K_1, is defined as min^{-1}. Fig. 13b shows the linear trend of $\log(q_e - q_t)$ with time, from which the values of K_1 and q_e can be determined by calculating their slope and intercept, respectively.

According to the plot model below, the PFO concept aligns well with the practical data. The PSO concept is described by the equation below (eqn (6)).[59]

$$\frac{t}{q_t} = \frac{1}{k_2 {q_e}^2} + \frac{t}{q_e} \quad (6)$$

k_2 is a fixed rate, and it's given in g mg^{-1} min^{-1}. A slope of $1/k_2{q_e}^2$ and an interception of $1/q_e$ make up the equation. The PSO can be applied to real-world data, as illustrated in Fig. 13c. When describing chemisorption processes, the Elovich concept is frequently employed, particularly for systems with

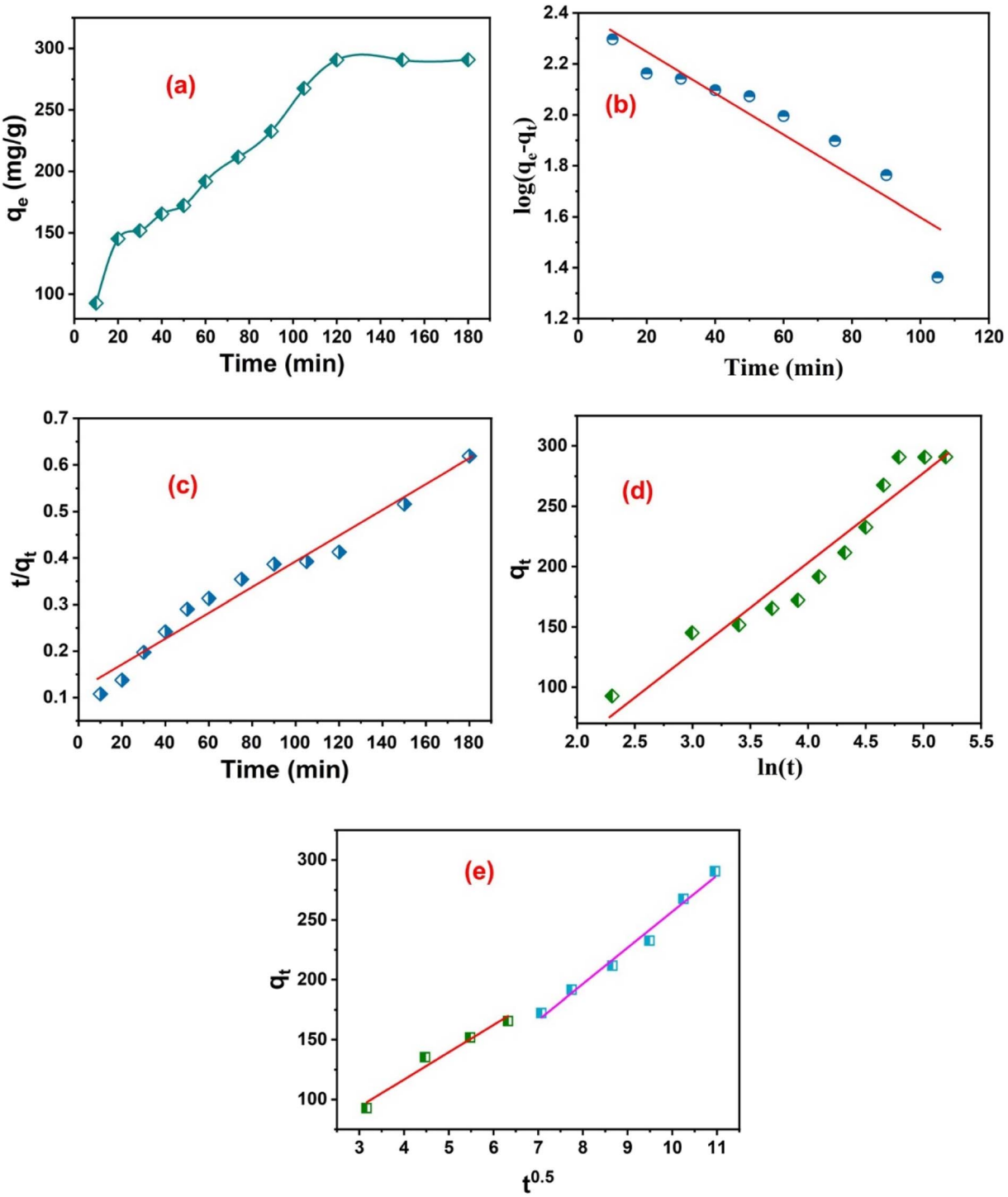

Fig. 13 (a) Time result of Li^+ adsorption, (b) PFO, (c) PSO, (d) Elovich, (e) IPD types of Li^+ adsorption on CNT–AMP (600 mg L^{-1} Li^+, 50 mL, pH 12, 120 minutes, 0.08 g CNT–AMP, 25 °C).

heterogeneous surfaces and slow sorption rates. It works particularly well for adsorption processes where the adsorbate and adsorbent have varying binding energies and complicated surface interactions.[60] This model's adaptability makes it useful in many situations when the sorbent surface shows a wide variety of binding site affinities and irregular activity. Eqn (7) yields a numerical description of this paradigm.

$$q_t = \left(\frac{1}{\beta}\right)\ln(\alpha\beta) + \left(\frac{1}{\beta}\right)\ln t \quad (7)$$

The desorption constant, β, is proportional to the surface coverage and the activating energy for chemisorption, and α is the initial sorption rate in milligrams per gram per minute. The relationship between q_t and ln t, as shown in Fig. 13d, was used

Table 1 Kinetic aspects governing Li^+ adsorption on CNT–AMP

PFO				PSO		
K_1	$q_{e,cal}$	R^2	$q_{e(exp)}$	k_2	$q_{e,cal}$	R^2
1.86×10^{-3}	243.82	0.8806	292.17	0.001	294.12	0.9874

Elovich			IPD			
α	β	R^2	k_d (mg g^{-1} $min^{-0.5}$)		C	R^2
20.934	0.013	0.9234	1st stage	22.824	25.402	0.9652
			2nd stage	30.215	45.064	0.9846

to find the constants α and β. According to the equation, the slope is equal to $1/\beta$, and the intercept is $(1/\beta)\ln(\alpha\beta)$.[61] Eqn (8) provides the model for the IPD kinetics.

$$q_t = k_d t^{0.5} + C \quad (8)$$

Li^+ sorption at time t, denoted as q_t, is given by the equation where k_d is the diffusion rate constant in mg g^{-1} $min^{-0.5}$, and C is the thickness of the boundary zone. Four well-established simulations were used to assess the kinetic response of lithium-ion binding onto the CNT–AMP adsorbent. The kinetic parameters that were obtained from every single model are listed in Table 1. The PSO version showed the best agreement with the experimental information, as indicated by the largest coefficient of correlation (R^2) among the hypotheses that were evaluated. The model's computed adsorption capacity ($q_{e,cal}$) also agreed strongly with the experimentally determined value (q_{exp}), lending credence to its usefulness. Alternatively, the PFO version did not provide an accurate description of the adsorption process, as it produced a $q_{e,cal}$ that was significantly lower than the actual q_{exp} and had a lower R^2 value than the other models. The results show that the PSO model is the most accurate description of the Li^+ adsorption kinetics onto CNT–AMP. This model suggests that the rate-limiting phase is controlled by chemisorption on the surface of CNT–AMP.

Applying the IPD model enables experts to delve further into the adsorption process and identify the driving force: surface contact or diffusion into the pores. Others can see the resultant graph in Fig. 13e. The only rate-limiting process, with negligible boundary layer resistance, would be intra-particle diffusion, according to a linear plot that passes through the origin. Fig. 13e illustrates a two-step process, and the linear regions that comprise each stage have their own unique R^2 coefficients and rate factors. Fast adsorption on the surface and exterior transfers of mass characterize the initial phase, as characterized by the rate variable k_{d1}.[62]

The next step involves weaker diffusion-controlled sorption in the adsorbent matrices and has the rate value k_{d2}. The rates of diffusion drop as the transport of ions becomes increasingly obstructed, approaching saturation, and surface sites become less available.

The kinetic results shown in Table 1 support this idea; k_{d2} is always less than k_{d1}, indicating that diffusion restriction plays a role in the last stage of binding.[63]

3.5. Initial Li^+ concentration consequence and sorption isotherms

Under the ideal circumstances (120 minutes, pH 12), the CNT–AMP material's adsorption activity was assessed concerning different starting levels of Li^+ ions, which ranged from 250 to 1400 mg L^{-1}. The adsorption ability of Li^+ rose steadily with increasing starting concentrations until reaching a state of saturation plateau at 1400 mg L^{-1}, as shown in Fig. 14a.

At the point when all binding locations on the CNT–AMP layer were fully occupied, this plateau was formed. The removal effectiveness is reduced after saturation is reached because there is increased competition among the ions for the restricted adsorption sites with larger amounts of Li^+ ions in solution.[64] However, the association between the starting level of Li^+ and the ability to adsorb the capability of the CNT–AMP substance is directly demonstrated by the data. Higher ionic concentrations provide a stronger driving force, which aids in overcoming the mass transfer restrictions between the solution and the CNT–AMP surface. Consequently, the material's overall loading capacity is improved because there is a higher probability of productive interactions with Li^+ ions and the active sites for adsorption.[65]

To develop and optimize effective adsorption frameworks or determine a material's highest adsorption capacity, it is essential to understand adsorption isotherms. This work utilized four popular isotherm frameworks to analyze the equilibrium data: Langmuir, Freundlich, Temkin, and Dubinin–Radushkevich (D–R) approaches. Adsorption occurs uniformly on a homogeneous surface through monolayer coverage, as there are no interactions between adsorbed molecules. These assumptions form the basis of the Langmuir model. This is the linearized Langmuir phenomenon, as shown by eqn (9):[66]

$$\frac{C_e}{q_e} = \frac{1}{q_m K_L} + \frac{C_e}{q_m} \quad (9)$$

When the flow of energy of the sites of adsorption varies along the outermost layer of a heterogeneous material, the Freundlich isotherm hypothesis (eqn (10)) is used to characterize the adsorption process.[67,68] Eqn (11), the Temkin isotherm, on the other hand, takes the adsorbate–adsorbent

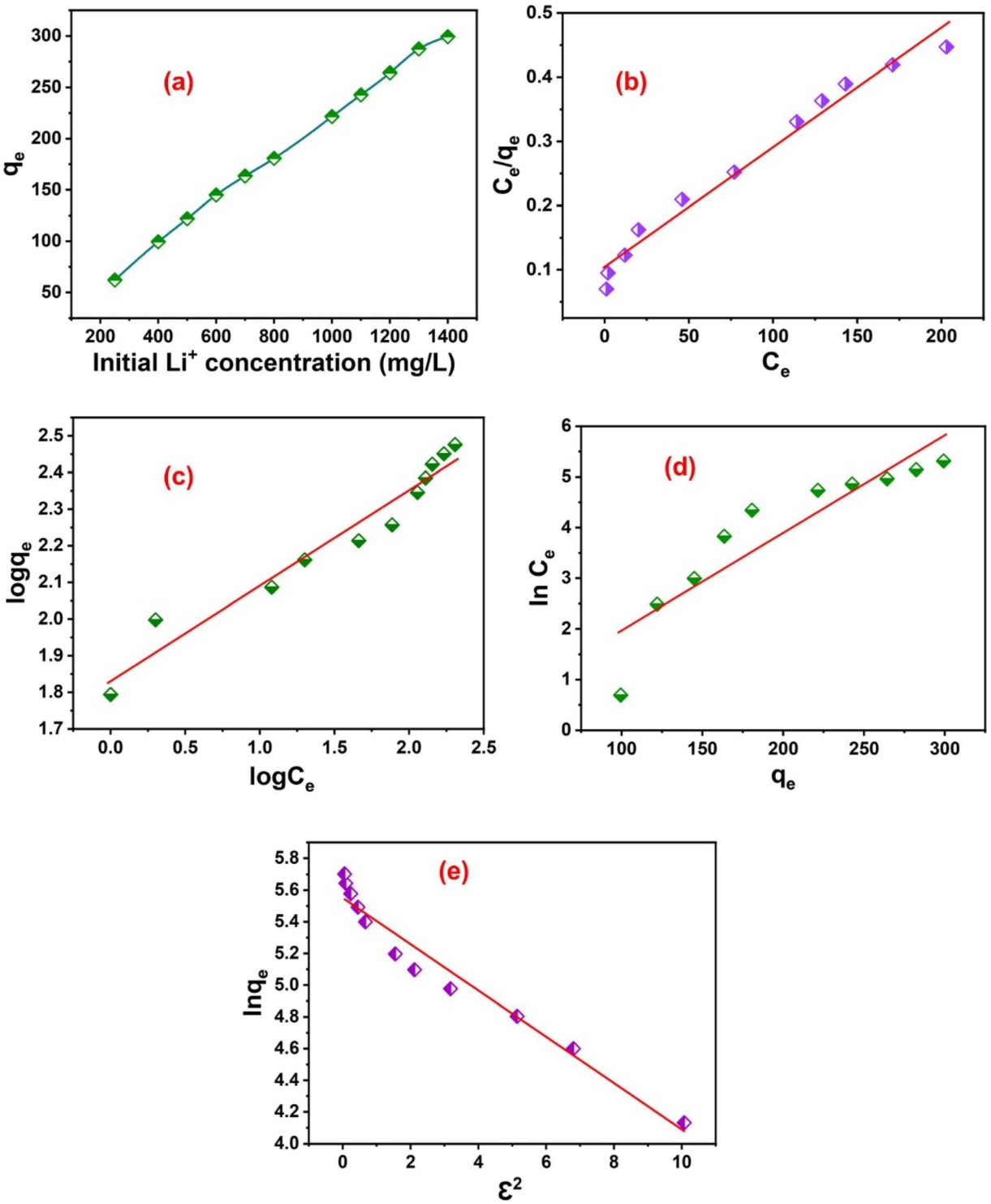

Fig. 14 (a) Initial lithium concentration, isotherm model of Li^+ adsorption using CNT–AMP (b) Langmuir, (c) Freundlich, (d) Temkin, and (e) D–R.

interaction-based linear decrease of the thermal energy of adsorption as an assumption.[69]

$$\log\ q_e = \log K_f + \frac{1}{n}\log C_e \quad (10)$$

$$q_e = \frac{RT}{b_T}\ln A_T + \frac{RT}{b_T}\log C_e \quad (11)$$

In all isotherm models, q_e denotes the equilibrium adsorption capacity of Li^+ on CNT–AMP (mg g^{-1}), and q_m is the maximum monolayer adsorption capacity obtained from the Langmuir fit (mg g^{-1}). C_e represents the equilibrium concentration of Li^+ in solution (mg L^{-1}). For the Langmuir model, K_L is the Langmuir affinity constant (L mg^{-1}); for the Freundlich model, K_F is the Freundlich constant related to sorption capacity, and n is the

heterogeneity factor; and for the Temkin model, K_T is the Temkin equilibrium binding constant (L g^{-1}) and b_T is the Temkin constant associated with the heat of adsorption.

The Langmuir approach utilizes the variables K_L and q_m to describe the affinity constant of the binding sites and the theoretical maximum monolayer adsorption capacity, respectively, expressed in units of L mg^{-1} and mg g^{-1}. Both C_e and q_e are measures of equilibrium; C_e is the level of lithium ions in the liquid in milligrams per liter, while q_e is the quantity of Li^+ attracted per gram of CNT–AMP. As it pertains to the Temkin model, the variables A_T (binding constant/gram), R (universal gas constant), T (absolute temperature/kelvin), and b_T (adsorption heat variation/kelvin) are all crucial. The Dubinin–Radushkevich (D–R) isotherm, which determines the mean independent energy of sorption (E) according to eqn (12), is useful for differentiating between ion exchange, mechanical adsorption, and chemisorption, among other adsorption strategies.

$$\ln q_e = \ln q_d - B_D(\varepsilon)^2 \quad (12)$$

To further aid in predicting the kind of adsorption from the initial lithium concentration C_0, eqn (13)[70] provides the dimensionless separating coefficient R_L. When the value of the R_L parameter is larger than 1, it implies unfavorable adsorption; when it is between 0 and 1, it suggests favorable adsorption; and when it is less than 0, it indicates irreversible retention.[71] This investigation confirms a highly favorable adsorption procedure, with R_L values for CNT–AMP ranging from 0.01 to 0.04.

$$R_L = \frac{1}{1 + K_L C_0} \quad (13)$$

It was discovered that the ability to absorb water of the CNT–AMP material was directly related to the initial amount of Li^+ ions. Fig. 14 and Table 2 display the outcomes of the experimental data analysis performed using the Langmuir, Freundlich, Temkin, and D–R isotherm systems. The strongest correlation value was seen in the Langmuir model, which indicates that Li^+ adsorption occurs on surfaces with homogeneous energy sites through a monolayer adsorption pathway.[72] At ambient temperature and pH 12, CNT–AMP achieved a maximum predicted adsorption capability of 303.03 mg g^{-1} as determined by the Langmuir criteria. This agreement with the experimental data is quite good, indicating that the Langmuir model is a suitable fit for the data and that functional group couplings are crucial for enhancing adsorption capacity.

Despite its consideration, the Temkin approach failed to adequately fit the experimental information, most likely because it assumes homogeneous surfaces, as indicated by the reduced correlation ratio. Fig. 14d shows that the binding energy (A_T) was found to be 10.188 L g^{-1} and that the constant b, which is linked to adsorption heat, was computed as 54.01 kJ mol^{-1} in this framework. In addition, the computed mean energy of adsorption E of 10.684 kJ mol^{-1} and an elevated correlation value ($R^2 = 0.9599$) provide significant evidence for chemisorption, confirming the D–R isotherm model. The D–R model is a good fit for explaining the attraction of lithium ions over CNT–AMP, as shown by these results.

Table 2 Adsorption isotherm parameters for Li^+ ions on CNT–AMP

Isotherm simulations	Variables	
Langmuir	Eq.	$y = 0.0033x + 0.1046$
	q_m (mg g^{-1})	303.03
	K_l	0.03155
	R^2	0.9859
Freundlich	Eq.	$y = 0.2608x + 1.8301$
	K_f (mg g^{-1})	67.624
	$1/n$ (mg min g^{-1})	0.2608
	R^2	0.9427
Temkin	Eq.	$y = 0.0193x + 0.0448$
	A_T (L m^{-1})	10.188
	b_T	54.01
	R^2	0.8313
D–R	Eq.	$y = -0.0044x + 5.6946$
	q_D (mg g^{-1})	297.26
	B_D (mol^2 kJ^{-2})	0.0051
	E_D (kJ mo1^{-1})	10.684
	R^2	0.9599
Practical capability	q_{exp} (mg g^{-1})	299.25

3.6. Thermodynamics study

At temperatures ranging from 298 to 343 K and starting concentrations of 1400 mg L^{-1}, the effects of elevated temperatures on Li^+ deletion were studied. Due to faster mass exchange and stronger adsorbate relationships, CNT–AMP was able to obtain a larger Li^+ adsorption capacity at elevated temperatures (Fig. 15a). The Li^+ adsorption framework onto CNT–AMP was better understood by calculating thermal parameters employing the van't Hoff plot (Fig. 15b). The enthalpy change (ΔH°), entropy change (ΔS°), and Gibbs energy-free change (ΔG°) were derived from eqn (14) and (15), respectively. Table 3 shows that in the circumstances tested, the act of adsorption happens spontaneously due to a negative reading of ΔG°.[73]

The isothermal adsorption information (Fig. 15b) further supports the finding that the capacity of adsorption improves with higher temperatures, which is further confirmed by the positive ΔH° value, which in turn implies that the adsorption step is endothermic.[74] Also, because of the restructuring of structures and the release of molecules of solvent, a positive reading of ΔS° during sorption suggests a boost in disorder at the solid–liquid interface.[75] The thermodynamic findings provide strong evidence that the uptake of Li^+ by CNT–AMP is an endothermic, spontaneous, and entropy-driven process. Eqn (14) and (15) were used to systematically derive the evaluated thermodynamic variables.

The temperature dependence of the equilibrium distribution coefficient, K_d, defined in eqn (3), was used to determine the thermodynamic parameters of Li^+ adsorption. By plotting $\log K_d$ as a function of $1/T$, the standard enthalpy and entropy changes of the process were obtained from the van't Hoff relationship

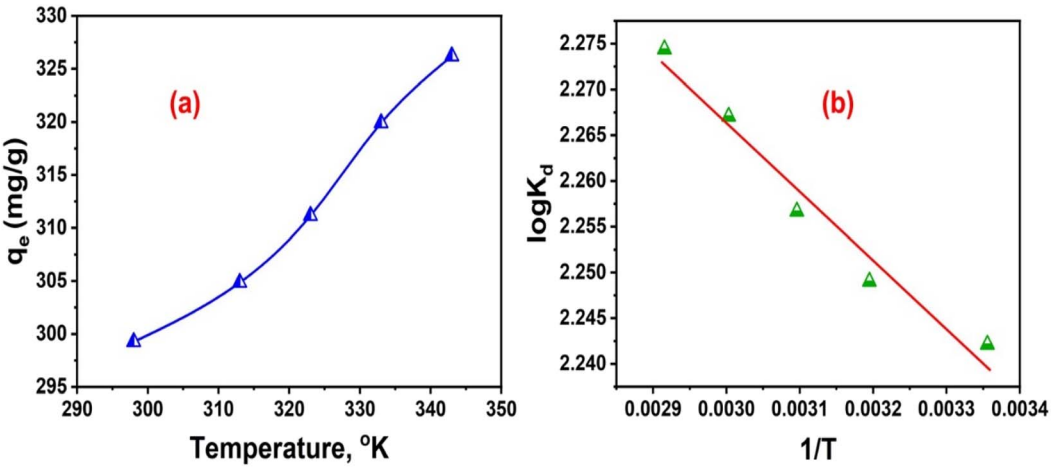

Fig. 15 (a) Temperature consequence on Li^+ adsorption on CNT–AMP, (b) plot of log K_d *vs.* 1/*T*, (1400 mg L^{-1} Li^+, 50 mL, pH 12, 120 minutes, 0.08 g CNT–AMP, 25 °C).

Table 3 Thermodynamic aspects for Li^+ sorption on CNT–AMP

$\Delta H°$ (kJ mol^{-1})	$\Delta S°$ (J mol^{-1} K^{-1})	$\Delta G°$ (kJ mol^{-1})				
		298 K	313 K	323 K	333 K	343 K
1.441	47.715	−12.61	−13.32	−13.79	−14.26	−14.73

(eqn (14)). In this context, K_d represents the equilibrium partition of Li^+ between the solid CNT–AMP phase and the liquid phase, and it is not a kinetic rate constant.

$$\log K_d = \frac{\Delta S°}{2.303R} - \frac{\Delta H°}{2.303RT} \quad (14)$$

$$\Delta G = \Delta H - T\Delta S \quad (15)$$

3.7. Comparative evaluation of lithium adsorption capacities

Table 4 shows the results of a comparison between the CNT–AMP composite and various other adsorbent compounds as it pertains to lithium adsorption. Without a doubt, the CNT–AMP surpassed all the competing materials with its greatest lithium adsorption capacity of 299.25 mg g^{-1}. To illustrate, LIIMsTiO_2@PVDF adsorbed 132 mg g^{-1}, while Li-imprinted polymers (Li-IIPs) and SiO_2@SP-PDAIIM composites demonstrated capacities of 250 mg g^{-1} and 231 mg g^{-1}, respectively. Alternatively, H_2TiO_3 and its modified derivatives H_2TiO_3–Zr and H_2TiO_3–Mo demonstrated significantly poorer performances, varying from 76.7 to 93.2 mg g^{-1}. The sorption capacity was much lower, reported at 54.65 mg g^{-1}, for biopolymer-based adsorbents such as chitosan-HMO. The rapid absorption of CNT–AMP in acidic circumstances is probably caused by its huge functional surface area, its abundance of AMP functional structures, and its strong selective binding for Li^+ ions. When these characteristics work together, they improve binding site accessibility and ion exchange interactions. These results demonstrate that CNT–AMP is a highly effective binder for lithium recovery, even from complicated solutions like spent lithium-ion battery leachates.

3.8. Selective Li-ion adsorption on CNT–AMP with coexisting competitive cations

The capacity of CNT–AMP to preferentially adsorb Li^+ even when other cations are present is crucial for its practical use in lithium recovery from complicated aqueous matrices. To evaluate the material's competitive adsorption behavior, this important performance characteristic was tested with synthetic brine solutions that contained 250 mg L^{-1} of Li^+, Na^+, K^+, Ca^{2+}, and Mg^{2+} (Fig. 16). The experimental results showed that the presence of competing cations reduced the effectiveness of lithium adsorption; however, the strength of this effect differed according to the ionic properties of the individual coexisting ions. Because their ionic radius is extremely similar to that of Li^+ (0.067 nm *vs.* 0.06 nm), magnesium ions were the most competitive. Due to the high hydration energy of Mg^{2+}, efficient competition at the adsorption contact is prevented. This is because the thermodynamic advantage derived from adsorption

Table 4 Comparison of the excessive uptake ability of Li^+ by CNT–AMP with further declared adsorbents

Adsorbent material	Capacity (mg g^{-1})	Ref.
LIIMsTiO_2@PVDF	132	76
SiO_2@SP-PDAIIM	231	77
SP-IIMs	42.58	78
Chitosan – HMO	54.65	79
H_2TiO_3	76.7	80
Li-IIPs	250	81
H_2TiO_3–Zr	93.2	82
H_2TiO_3–Mo	78	83
CNT–AMP	**299.25**	**This study**

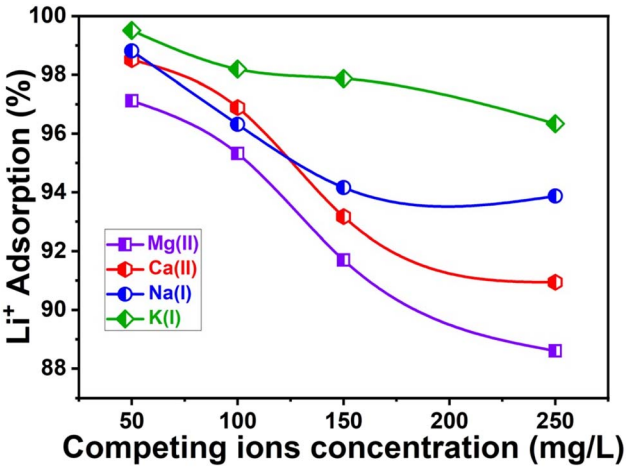

Fig. 16 Competing ions' impact on the adsorption efficiency of Li^+ on CNT–AMP.

is outweighed by the energy needed to dehydrate and bind to the sites of activity on CNT–AMP.[84]

Although divalent as well, the inhibitory action of calcium ions (Ca^{2+}) was less pronounced. Their mobility and selectivity for CNT–AMP are hindered by their larger radius and more powerful hydration shell, which limits their capacity to occupy adsorption sites allocated to Li^+. However, due to their bigger ionic diameters and lower electrostatic bonds with the functioning adsorbent surface, monovalent ions like Na^+ and K^+ had little impact on lithium uptake.[85] No matter how tough the competition was, CNT–AMP still managed to show impressive lithium absorption capabilities. The material's ability to retain outstanding performance under typical multi-component situations was demonstrated by the fact that lithium adsorption was slightly reduced from 250 mg g^{-1} to 220.1 mg g^{-1} when other ions were present. Multiple interacting factors contribute to this improved selectivity. Ions with larger radii and stronger hydration shells have a harder time adsorbing than smaller ones due to steric hindrance and differences in hydration energy. The second reason is that tiny, less hydrated cations like Li^+ can form stronger binding contacts with CNT–AMP due to its surface chemistry, especially its phosphonate-modified active sites. Competing with larger or more strongly hydrated species is likely discouraged by the optimum electrostatic conditions provided by these active sites.

When taken as a whole, these results highlight CNT–AMP's promise as an effective and selective adsorbent for extracting lithium from salty sources. Since coexisting ions do not affect lithium recovery, CNT–AMP is a material that shows promise for large-scale methods that aim to separate lithium from complex brine systems.

In real wastewater and battery-recycling streams, the inorganic matrix is often accompanied by organic additives and trace heavy metals, which may influence the performance of CNT–AMP. The aminomethylenephosphonate groups that decorate the CNT surface are hard oxygen donors that preferentially coordinate small, hard cations such as Li^+; however, strongly complexing transition metals (for example, Cu^{2+} or Ni^{2+}) could compete with Li^+ for these sites when present at sufficiently high concentrations. By contrast, neutral or weakly polar organic molecules are more likely to induce surface fouling or partial blockage of the mesoporous structure than to form specific complexes with the phosphonate groups. For practical deployment in complex effluents, CNT–AMP is therefore best integrated into a treatment train that includes upstream removal of strongly chelating heavy metals and, where necessary, periodic regeneration to mitigate organic fouling. Systematic interference tests with representative organic additives and heavy metals will be the focus of future work to delineate these effects quantitatively.[86]

3.9. Regeneration performance of CNT–AMP adsorbent

For large-scale applications to be economically viable and ecologically sustainable, the regeneration capability of adsorbent materials is crucial. A thorough desorption investigation was conducted using several chemical agents to evaluate the reusability of the CNT–AMP adsorbent. Solutions of various acids, bases, and neutrals were included, including NaOH, NaCl, $Ca(NO_3)_2$, HCl, KNO_3, HNO_3, and chelating agents such as EDTA, and disodium EDTA (Na_2EDTA). The agents were tested at a concentration of 0.1 M in a controlled environment, with a 60-minute contact time at 25 °C. After that, the CNT–AMP adsorbent was rinsed thoroughly with deionized water and reapplied.

Based on the comparison findings presented in Fig. 17a, nitric acid had the best desorption performance for Li^+ recovery from CNT–AMP among the eluents evaluated. By keeping the desorption parameters constant, we were able to maximize the elution efficiency of HNO_3 by studying its concentration range of 0.1 M to 1 M. The results show that the best lithium desorption efficiency is achieved with 0.25 M HNO_3, which means that larger acid concentrations may not improve recovery but could damage the adsorbent's structure or functional activity (Fig. 17b).

Additionally, to determine the optimal recovery time, researchers systematically examined the effect of desorption contact time, ranging from 30 to 180 minutes. Fig. 17c shows that after 120 minutes, the Li^+ recovery was almost completely depleted, and after that point, there was no more improvement. Based on these results, the best conditions for CNT–AMP adsorbent regeneration are a 120 minute desorption cycle with 0.1 M HNO_3 at room temperature.

In summary, the exceptional recovery performance, especially when a weak nitric acid solution is present, showcases the durability and reusability of CNT–AMP in multiple adsorption–desorption cycles. Due to these features, it is more suitable for long-term lithium recovery activities in settings with limited resources or on an industrial scale. Using 0.25 M HNO_3 as the eluent for 120 minutes per cycle, the regeneration performance of the CNT–AMP adsorbent was tested over nine consecutive adsorption–desorption cycles. Adsorption exceeded 95% in the first two cycles, demonstrating that the adsorbent maintained virtually 100% lithium-ion removal efficiency initially. However,

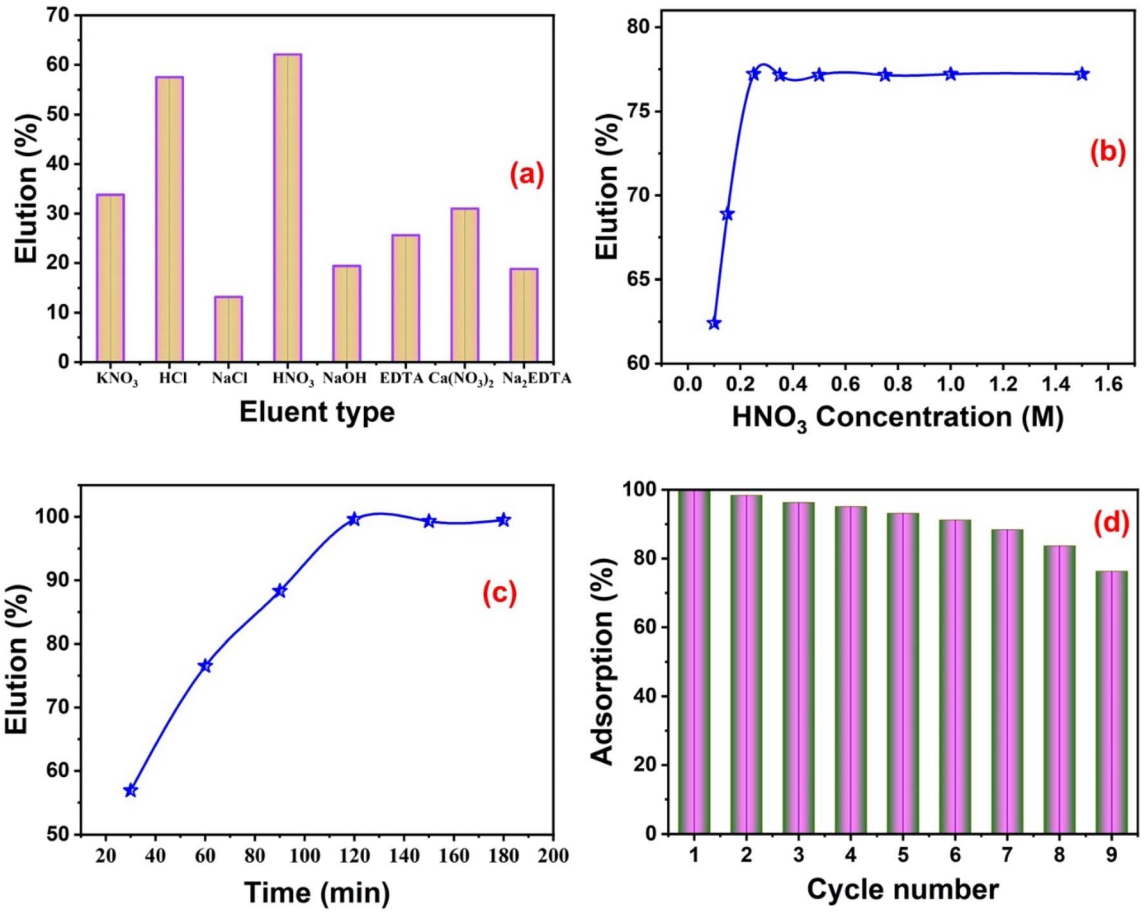

Fig. 17 (a) Numerous eluting agents outcome, (b) HNO_3 concentration outcome, (c) eluting time of lithium from CNT–AMP, and (d) recycling ability of CNT–AMP for Li^+.

with each regeneration phase, performance gradually declines. The adsorption effectiveness dropped to about 75% by the ninth cycle, suggesting that the CNT–AMP framework had either slightly degraded structurally or lost a cumulative amount of active binding sites due to the acid treatment. This decrease is hardly surprising, given the adsorbent's remarkable stability and reusability, as it continues to retain a high degree of lithium-ion absorption even after multiple applications. This trend suggests that CNT–AMP has the potential to be utilized in lithium recovery processes with minimal regeneration losses, indicating it could be a viable option for sustainable and affordable resource recovery systems (Fig. 17d).

3.10. Tentative adsorption mechanism

At pH 12, every aminophosphonate headgroup on CNT–AMP is fully deprotonated to $-PO_3^{2-}$, creating a densely negative surface that strongly attracts Li^+ from the solution (Fig. 18). As Li^+ diffuses toward the CNT–AMP, it partially sheds its hydration shell (*e.g.*, retaining one or two water molecules) so that it can fit into a multi-donor coordination environment. Each Li^+ is chelated by two phosphonate oxygens, each belonging to a different CNT–AMP chain, with one residual water (and, in some pockets, a nearby carbonyl oxygen or amine N) completing a three- or four-coordinate sphere around Li^+. Any fleeting $-PO_3H^-$ species immediately undergoes ion exchange ($-PO_3H^- + Li^+ \rightarrow -PO_3(Li)^- + H^+$), but under strongly alkaline conditions, this step is essentially complete before full chelation.

It should be noted that the coordination scenario proposed in Fig. 18 is still tentative and is derived from the combined analysis of FT-IR, XPS, and adsorption behavior, rather than from direct structural probes of the Li^+ environment. In the present work, neither EXAFS nor solid-state NMR data are available, and no DFT calculations have yet been performed. Future studies will therefore focus on combining advanced spectroscopy with atomistic modelling to refine the local coordination geometry of Li^+ on CNT–AMP and to quantify the energetic contributions that underpin its selectivity over competing cations. This will allow the qualitative mechanism proposed here to be translated into a fully validated, molecular-level description.

The interaction between Li^+ and CNT–AMP is depicted at the atomic level, with Li^+ coordinated by two to three oxygen atoms from neighboring deprotonated phosphonate groups ($-PO_3^{2-}$) tethered to the CNT backbone and, when sterically accessible, by a nearby nitrogen donor. This chelating arrangement is consistent with the XPS evidence for Li^+ association with P/O

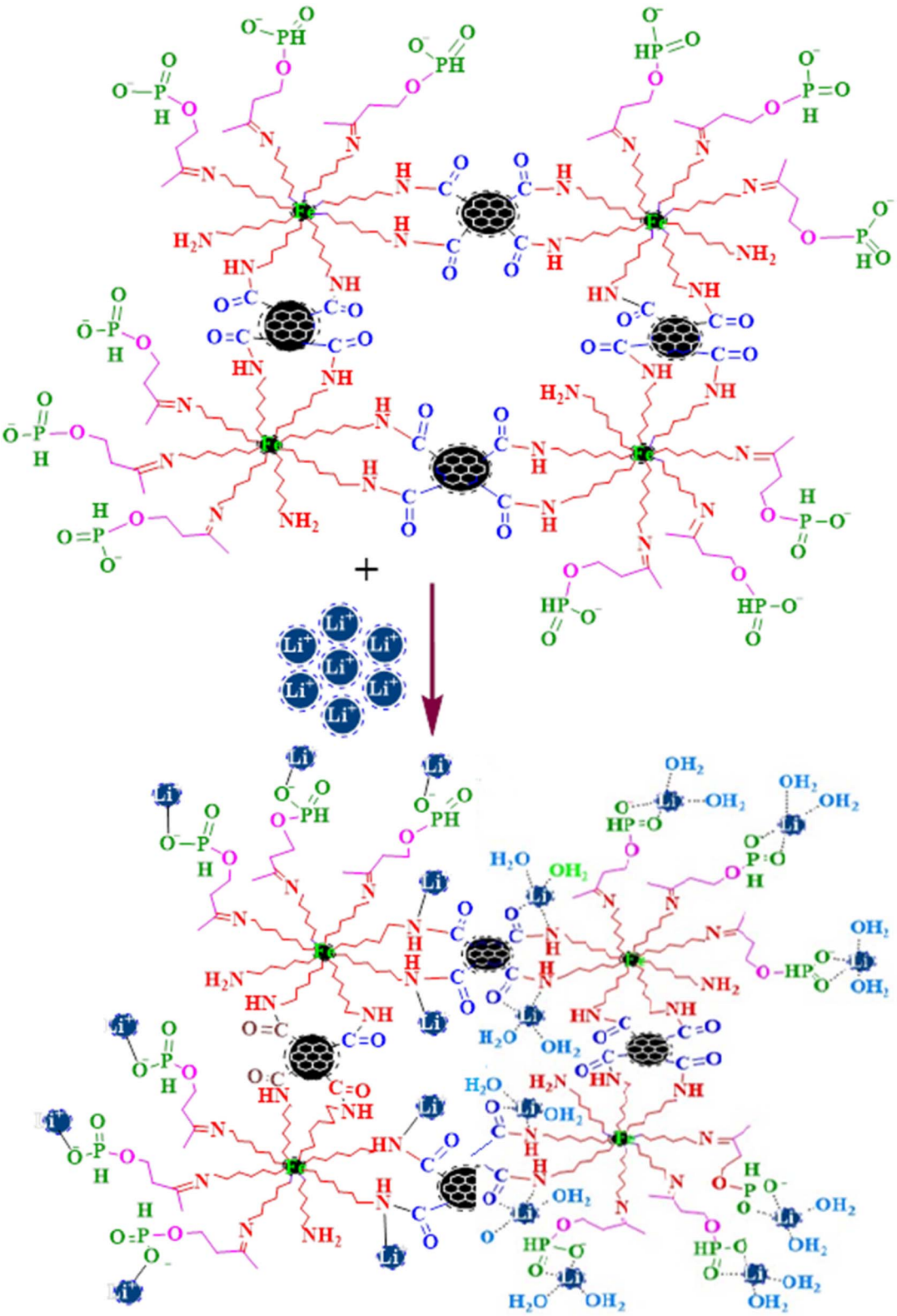

Fig. 18 Proposed atomic-scale coordination environment of Li^+ on CNT–AMP.

environments and with the chemisorption-type behavior inferred from the thermodynamic analysis, while still acknowledging that the exact geometry remains to be confirmed by advanced structural methods.

The net result is a thermodynamically favored, multi-dentate Li–O coordination that overcomes the dehydration penalty and anchors Li^+ within the mesoporous network. XPS confirms this binding mode: the P 2p peak shifts from ~132.8 eV to ~133.2 eV

upon Li^+ complexation, and the N 1s feature shifts from ~399.6 eV to ~400.1 eV, consistent with minor Li–N polarization adjacent to the phosphonate. Because Li^+ ($r \approx 0.76$ Å, $\Delta H_{hyd} \approx -520$ kJ mol^{-1}) is easier to desolvate and fits snugly into these O-rich chelate pockets than competing cations (*e.g.*, Mg^{2+}, Ca^{2+}), CNT–AMP exhibits excellent Li^+ selectivity and high uptake capacity at pH 12.

3.11. Application of CNT–AMP in lithium adsorption from spent Li-ion batteries

Lithium ions (Li^+) were extracted from $LiCoO_2$ (ICR) cathodes found in lithium-ion batteries that were recycled from old laptops bought from secondhand stores and electronics repair shops.

The process started with the hand removal of the plastic housing that encased the battery cells. A sodium chloride (NaCl) solution containing 5% (w/v) was used to submerge the cells for a full day to prevent electrical short-circuiting. The cells were then dried in a 90 °C oven for 12 hours after a thorough rinsing with deionized water. Then, the metal covers of each cell were cut open by hand. After delicately removing the exterior steel shell, the inside components were separated into plastics, cathode sheets made of aluminum, and anode sheets made of copper. To effectively separate the cathodic powder, the aluminum sheets were heated to temperatures ranging from 250 to 300 °C for 30 minutes, thermally delaminating the active cathode material. A consistent particle size of fewer than 200 μm was achieved by milling and sieving the recovered material.

According to eqn (16),[87] sulfuric acid and a reducing agent (hydrazine sulfate) were used to leach the $LiCoO_2$ cathode powder.

$$4LiCoO_2\,(s) + 5H_2SO_4\,(aq) + N_2H_6SO_4\,(aq) \rightarrow 4CoSO_4\,(aq) + 2Li_2SO_4\,(aq) + 8H_2O\,(g) + N_2\,(g) \quad (16)$$

Table 5 summarizes the results of the inductively coupled plasma optical emission spectrometry (ICP-OES) that were used to determine the amounts of cobalt and lithium in the filtrate after filtering the resultant leachate to separate the solid residue. Ammonium oxalate was employed as the precipitating agent to selectively recover cobalt from the leach solution. To achieve the precise reaction conditions described by the stoichiometric reaction in eqn (17), the pH was adjusted to 1.5, the stirring speed was kept at 300 rpm, and the temperature was maintained at 75 °C for 60 minutes.

$$Li^+\,(aq) + Co^{2+}\,(aq) + (NH_4)_2C_2O_4\,(aq) \rightarrow CoC_2O_4\,(s) + Li^+\,(aq) + 2NH_4^+\,(aq) \quad (17)$$

The selective precipitation of cobalt is made possible by ammonium oxalate's dual role as a complexing and precipitating agent. Isolation of the solid was achieved by filtering, followed by extensive washing to eliminate any remaining contaminants, and finally, drying. Utilizing scanning electron microscopy in conjunction with energy-dispersive X-ray spectroscopy (SEM-EDX), the precipitated cobalt oxalate was characterized.

Table 5 The detailed contents of different elements in the spent $LiCoO_2$ cathode material

Metal	Li	Co	Al	Mn	Ni
Content (wt%)	6.57	58.29	0.06	0.16	0.37

Fig. 19a displays the diffraction pattern obtained from XRD, which was used to conduct additional structural characterization of the recovered CoC_2O_4. Fig. 19b shows the equivalent micrographs of the surface morphology that was studied using SEM. The remaining leachate after cobalt removal mostly consisted of lithium ions with minor quantities of manganese, aluminum, and cobalt. The quantities of lithium in the filtrate were found to be 6389 mg L^{-1} and cobalt to be 176 mg L^{-1}. The next stage involved adding 250 mL of the cobalt-free leach solution to 1 gram of CNT–AMP adsorbent to selectively adsorb lithium. To make sure the adsorption conditions were ideal, the pH of the solution was measured and corrected to 12 with 1 M ammonium hydroxide (NH_4OH) or 1 M sulfuric acid (H_2SO_4). After being agitated for 120 minutes, the mixture reached a maximum efficiency of 98% for lithium adsorption. It uses 0.25 M nitric acid and maintained steady agitation at room temperature for 120 minutes to desorb the lithium-loaded CNT–AMP.

A precipitation stage utilizing sodium carbonate was employed to recover lithium after desorption. While stirring continuously at 60 °C, a stoichiometric amount of sodium carbonate (Na_2CO_3) was slowly added to the lithium-rich solution, keeping the pH at approximately 10. The white precipitate of Li_2CO_3 was filtered out, rinsed with deionized water to eliminate any remaining salts, and finally dried for future use or characterization.

According to the XRD pattern, the precipitate is cobalt oxalate, specifically, $CoC_2O_4 \cdot 2H_2O$, which is an orthorhombic crystal with a space group of Co(II)-oxalate (JCPDS file: 25-0250)[88,89] (Fig. 19a). The purity level of the compound is more than 98.7 percent, as confirmed by the ICP-OES analysis. Characteristic rod-like features, about 3 μm long, are visible in the precipitated product's morphology (Fig. 19b).

The Li_2CO_3 powder was dissolved in a 2mol L^{-1} H_2SO_4 solution and then analysed using ICP-OES and AAS to determine the lithium carbonate purity. The found Li_2CO_3 purity level of approximately 99.50% satisfies the Chinese production standard for Li_2CO_3 (GB/T 11075-2013: Li_2CO_3-0, Li_2CO_3 > 99.2%).[90] Fig. 20a shows the XRD pattern of the product. It fits the Li_2CO_3 standard card (PDF# 80-1307) with clearly defined crystalline diffraction peaks. According to the SEM picture (Fig. 20b), the Li_2CO_3 that has precipitated appears as aggregates of sheets with particles ranging from 5 to 8 micrometers in size.[91]

Based on the results of the ICP-MS analysis, which were presented in Table 6, the obtained Li_2CO_3 product complied with battery-grade specifications due to its high purity and excellent crystallinity. The product's purity reached 99.8 percent.

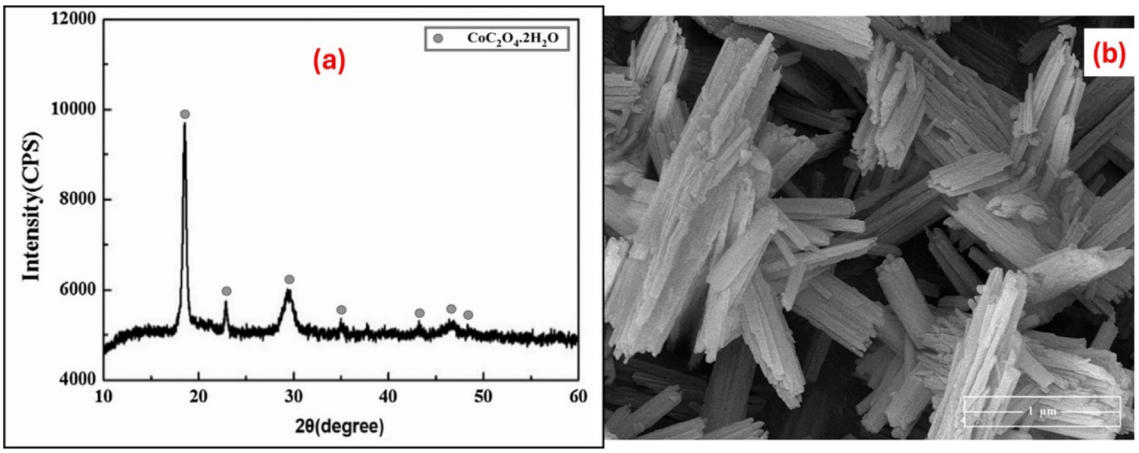

Fig. 19 (a) XRD evaluation and (b) SEM of CoC_2O_4 precipitate.

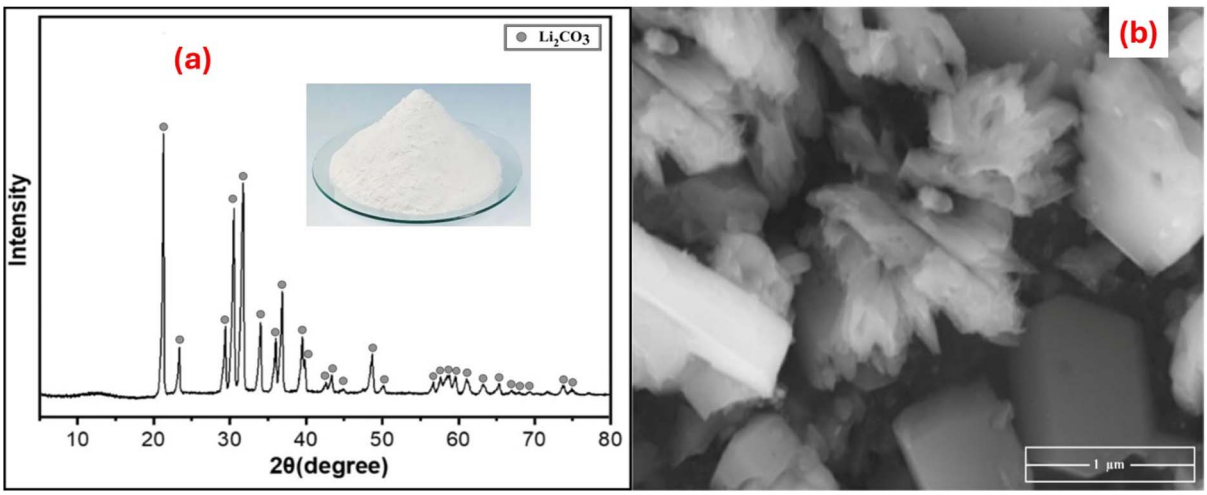

Fig. 20 (a) XRD exploration and (b) SEM of lithium carbonate precipitate.

Table 6 Chemical composition using ICP-OES of the Li_2CO_3 product

Element	Li	Ni	Co	Mn	Al
wt%	≥99.8%	≤0.012	≤0.001	≤0.001	≤0.040

4. Conclusion

This study introduces a new functionalized carbon nanotubes adsorbent (CNT–AMP) that is both efficient and sustainable for recovering lithium from used LIBs. Under ideal circumstances (pH 12, 25 °C, 120 min contact), the produced CNT–AMP achieved a maximum effectiveness of 299.25 mg g^{-1} in lithium adsorption, demonstrating outstanding performance. With recovery efficiency approaching 95.76% for lithium and 93.48% for cobalt, the adsorbent demonstrated exceptional selectivity for Li^+ ions, even when competing cations (Na^+, K^+, Ca^{2+}, Mg^{2+}) were present. This highlights the adsorbent's potential for practical uses in battery recycling. Extensive empirical and statistical evaluations were conducted to characterize the adsorption process. Kinetic investigations showed that the process follows PSO kinetics, establishing chemisorption as the major mechanism, and isotherm studies suggested that monolayer adsorption on homogenous active sites, with the Langmuir model providing the best fit. Positive entropy values suggest greater disorder at the solid–liquid interface during adsorption, while thermodynamic tests proved that adsorption is spontaneous and endothermic.

When applied to actual spent LIB leachates, CNT–AMP produced very pure lithium carbonate (Li_2CO_3) with a purity level of 99.8 percent. Using 0.25 M HNO_3 as an eluent, the adsorbent remained economically viable for large-scale applications after nine consecutive adsorption–desorption cycles, retaining more than 75% of its initial adsorption effectiveness. In addition to a practical method for recovering lithium from spent batteries, this study advances efforts to create long-term solutions for recycling valuable materials. Several benefits, such as increased efficiency, improved selectivity, less energy consumption, and less environmental impact, are offered by the

CNT–AMP adsorbent in comparison to traditional approaches. Potentially reshaping the way crucial metals are recovered from electronic waste, future studies might concentrate on improving the adsorbent for use in manufacturing and increasing the process's scale. Important implications for supporting principles of the circular economy in the battery business and addressing global lithium supply concerns are highlighted by this study's findings.

Author contributions

Mohamed E. Eissa: methodology, validation, data curation & interpretation, writing – original draft. Mohamed Abdel-Megid: methodology, validation, data curation & interpretation, writing – original draft, reviewing & editing. Bahig M. Atia: investigation, validation, data curation & interpretation, writing – original draft. Mohamed A. Gado: characterization, data curation & interpretation, writing – original draft, reviewing & editing. Mohamed F. Cheira: software, drawing chemical structures, data curation & interpretation, writing, reviewing & editing. Taha F. Hassanein: experimental operation, data interpretation, writing, reviewing & editing. Haeam A. Abdelmonem: experimental operation, data interpretation, writing, reviewing & editing.

Conflicts of interest

There are no conflicts to declare.

Data availability

All relevant data supporting the findings of this research are included within the manuscript. However, other data can be sent by the authors upon request.

Acknowledgements

This work was supported and funded by the Deanship of Scientific Research at Imam Mohammad Ibn Saud Islamic University (IMSIU) (grant number IMSIU-DDRSP2602).

References

1 Y. Han, S. Kim, S. Yu, N. V. Myung and H. Kim, *J. Ind. Eng. Chem.*, 2020, **81**, 115–123.
2 G. Han, D. Gu, G. Lin, Q. Cui and H. Wang, *Hydrometallurgy*, 2018, **177**, 109–115.
3 S. Jin, D. Mu, Z. Lu, R. Li, Z. Liu, Y. Wang, S. Tian and C. Dai, *J. Cleaner Prod.*, 2022, **340**, 130535.
4 H. Jiang, Y. Yang and J. Yu, *Sep. Purif. Technol.*, 2020, **241**, 116682.
5 B. K. Biswal, B. Zhang, P. Thi Minh Tran, J. Zhang and R. Balasubramanian, *Chem. Soc. Rev.*, 2024, **53**, 5552–5592.
6 Y. Sun, Q. Wang, Y. Wang, R. Yun and X. Xiang, *Sep. Purif. Technol.*, 2021, **256**, 117807.
7 E. H. Ang, Y. Z. Tan and J. W. Chew, *J. Mater. Chem. A*, 2019, **7**, 10206–10211.
8 Y. Feng, H. Peng and Q. Zhao, *Sep. Purif. Technol.*, 2022, **280**, 119848.
9 C. Liu, B. Tao, Z. Wang, D. Wang, R. Guo and L. Chen, *Chem. Eng. Sci.*, 2021, **229**, 115984.
10 X. Zhu, H. Yue, W. Sun, L. Zhang, Q. Cui and H. Wang, *Sep. Purif. Technol.*, 2021, **274**, 119099.
11 S. Choi, G. Hwang, S. Ilyas, Y. Han, N. V. Myung, B.-c. Lee, Y. Song and H. Kim, *Sep. Purif. Technol.*, 2020, **242**, 116757.
12 L. Liu, S. Liu, L. Zhao, G. Su, X. Liu, H. Peng, J. Xue and A. Tang, *J. Mol. Liq.*, 2020, **313**, 113593.
13 G. Zhang, C. Hai, Y. Zhou, W. Tang, J. Zhang, J. Zeng, Y. Liu, S. Dong and G. Peng, *Chem. Eng. J.*, 2022, **450**, 137912.
14 S. Liu, L. Liu, G. Su, L. Zhao, H. Peng, J. Xue and A. Tang, *React. Funct. Polym.*, 2022, **170**, 105127.
15 Q. Dong, H. Gang, J. Xu, Z. Li and Z. Wang, *J. Exp. Theor. Anal.*, 2024, **2**, 91–102.
16 M. Wiśniewska, G. Fijałkowska, I. Ostolska, W. Franus, A. Nosal-Wiercińska, B. Tomaszewska, J. Goscianska and G. Wójcik, *J. Cleaner Prod.*, 2018, **195**, 821–830.
17 B. Lin, G. Liu, Z. Zheng, H. Shi, M. Zhang, X. Yuan, Y. Huang, R. Li and C. Tang, *J. Environ. Chem. Eng.*, 2025, **13**, 116604.
18 P. Guo, Y. Wu, X. Ma, R. Chen, Z. Zeng, L. Li, C. Su and S. Wang, *Appl. Surf. Sci.*, 2025, **708**, 163754.
19 L. G. dos Santos, L. F. L. Machado, L. S. Andrade, G. T. M. Xavier, D. Mandelli and W. A. Carvalho, *Energy Environ. Sustainability*, 2025, **1**, 100031.
20 J. Li, L. Li, j. Fei, P. Zhao, J. zhao and Y. Xie, *Microchem. J.*, 2024, **200**, 110426.
21 C. Wang, X. Cheng, K. H. Luo, K. Nandakumar, Z. Wang, M. Ni, X. Bi, J. Zhang and C. Wang, *Mater. Sci. Eng., R*, 2025, **165**, 101010.
22 C. Xiao, J. Peng, Y. Jiao, Q. Shen, Y. Zhao, F. Zhao, H. Li and Q. Song, *Adv. Funct. Mater.*, 2024, **34**, 2409881.
23 B. Yan, Y. Shi, S. Liu, W. Wang, Z. Ba, H. Li, J. Wang, Z. Xiao, T. Peng, D. Liang and Y. Xie, *Sep. Purif. Technol.*, 2025, **374**, 133726.
24 M. Abe and N. Furuki, *Solvent Extr. Ion Exch.*, 1986, **4**, 547–565.
25 I. W. C. W. H. Tangkas, V. S. H. Sujoto, W. Astuti, S. N. A. Jenie, F. Anggara, A. P. Utama, H. T. B. M. Petrus and D. Sutijan, *J. Sustainable Metall.*, 2023, **9**, 613–624.
26 L. Chen, B. Tan, Y. Fang, L. Hu, J. Zhou, Y. Liang, J. Pan and J. Zhou, *Chem. Eng. J.*, 2025, **511**, 162274.
27 J. Zhong, S. Lin and J. Yu, *Sep. Purif. Technol.*, 2021, **256**, 117780.
28 T. Ryu, J. Shin, S. M. Ghoreishian, K.-S. Chung and Y. S. Huh, *Hydrometallurgy*, 2019, **184**, 22–28.
29 D. Sun, M. Meng, Y. Qiao, Y. Zhao, Y. Yan and C. Li, *Sep. Purif. Technol.*, 2018, **194**, 64–72.
30 N. Tran, H. W. Choi and Q. N. Tran, *Polymers*, 2024, **16**, 2848.
31 G. Zhang, J. Zhang, Y. Zhou, G. Qi, Y. Wu, C. Hai and W. Tang, *Colloids Surf., A*, 2019, **583**, 123950.
32 J. Ren, Z. Zhang, Z. Chen, L. Wan, K. Shi, X. Zeng, J. Li and Q. Liu, *Green Chem.*, 2023, **25**, 9795–9804.
33 L. Liu, W. Huang, H. Liang, Z. Su, K. Shi, J. Ren, L. Tan, Y. Min and Q. Liu, *Green Chem.*, 2025, **27**, 11870–11881.
34 Q. Zhao, C. Ding, J. Ren, Q. Liu, K. Shi and X. Zhan, *J. Environ. Chem. Eng.*, 2025, **13**, 120255.

35 O. A. Shabaan, H. S. Jahin and G. G. Mohamed, *Arabian J. Chem.*, 2020, **13**, 4797–4810.
36 H. Gao, X. Han, R. Wang, K. Zhu and R. Han, *Environ. Res.*, 2023, **231**, 116314.
37 H. Sadegh, G. A. M. Ali, A. S. H. Makhlouf, K. F. Chong, N. S. Alharbi, S. Agarwal and V. K. Gupta, *J. Mol. Liq.*, 2018, **258**, 345–353.
38 Y. Hu, C. Zou, T. Xiong and H. Wang, *J. Ind. Eng. Chem.*, 2023, **128**, 294–305.
39 Y. Yao, H. Chen, J. Qin, G. Wu, C. Lian, J. Zhang and S. Wang, *Water Res.*, 2016, **101**, 281–291.
40 M. A. P. Cechinel, S. M. A. G. Ulson de Souza and A. A. Ulson de Souza, *J. Cleaner Prod.*, 2014, **65**, 342–349.
41 Ş. S. Bayazit and İ. İnci, *J. Ind. Eng. Chem.*, 2013, **19**, 2064–2071.
42 L. Wang, J. Bao, L. Wang, F. Zhang and Y. Li, *Chem. - Eur. J.*, 2006, **12**, 6341–6347.
43 U. J. Kim, C. A. Furtado, X. Liu, G. Chen and P. C. Eklund, *J. Am. Chem. Soc.*, 2005, **127**, 15437–15445.
44 H.-H. Cho, K. Wepasnick, B. A. Smith, F. K. Bangash, D. H. Fairbrother and W. P. Ball, *Langmuir*, 2010, **26**, 967–981.
45 G. Quan, Q. Fan, J. Sun, L. Cui, H. Wang, B. Gao and J. Yan, *J. Hazard. Mater.*, 2020, **384**, 121265.
46 L. Wang, J. Wang, Z. Wang, C. He, W. Lyu, W. Yan and L. Yang, *Chem. Eng. J.*, 2018, **354**, 623–632.
47 M. Li, Y. Liu, C. Shen, F. Li, C.-C. Wang, M. Huang, B. Yang, Z. Wang, J. Yang and W. Sand, *J. Hazard. Mater.*, 2020, **389**, 121840.
48 S. M. Yakout, *Biorem. J.*, 2015, **19**, 171–182.
49 R. E. Elbshary, A. A. Gouda, R. El Sheikh, M. S. Alqahtani, M. Y. Hanfi, B. M. Atia, A. K. Sakr and M. A. Gado, *Int. J. Mol. Sci.*, 2023, **24**, 7423.
50 B. Zhang, Z. Qu, C. Ruiz-Agudo, L. Yang, B. Chi, Y. Kong and F. Wang, *Carbon*, 2025, **234**, 120020.
51 S.-W. Kim, S. Kwon and Y.-K. Kim, *Nanomaterials*, 2021, **11**, 288.
52 A. J. Pallenberg, K. S. Koenig and D. M. Barnhart, *Inorg. Chem.*, 1995, **34**, 2833–2840.
53 O. Nishikawa, M. Taniguchi and Y. Saito, *J. Vac. Sci. Technol.*, 2008, **26**, 1074–1078.
54 D. Gu, W. Sun, G. Han, Q. Cui and H. Wang, *Chem. Eng. J.*, 2018, **350**, 474–483.
55 P.-Y. Ji, Z.-Y. Ji, Q.-B. Chen, J. Liu, Y.-Y. Zhao, S.-Z. Wang, F. Li and J.-S. Yuan, *Sep. Purif. Technol.*, 2018, **207**, 1–11.
56 A. Khedri, D. Jafari and M. Esfandyari, *Arabian J. Sci. Eng.*, 2022, **47**, 6155–6166.
57 S. Zhuang, Q. Zhang and J. Wang, *J. Mol. Liq.*, 2021, **325**, 115197.
58 M. A. Gado, B. M. Atia, M. F. Cheira and A. A. Abdou, *Int. J. Environ. Anal. Chem.*, 2021, **101**, 1419–1436.
59 M. F. Cheira, *Int. J. Environ. Anal. Chem.*, 2021, **101**, 1710–1734.
60 B. M. Atia, H. A. Radwan, W. A. Kassab, H. K. A. Sarhan, M. A. Gado and A. E. Goda, *J. Chin. Chem. Soc.*, 2024, **71**, 507–522.
61 A. A. Alluhaybi, A. Alharbi, A. M. Hameed, A. A. Gouda, F. S. Hassen, H. S. El-Gendy, B. M. Atia, A. R. Salem, M. A. Gado, A. Ene, H. A. Awad and H. M. H. Zakaly, *Molecules*, 2022, **27**, 5087.
62 F. Zarei, A. Marjani and R. Soltani, *Eur. Polym. J.*, 2019, **119**, 400–409.
63 J. Liang, X. Li, Z. Yu, G. Zeng, Y. Luo, L. Jiang, Z. Yang, Y. Qian and H. Wu, *ACS Sustainable Chem. Eng.*, 2017, **5**, 5049–5058.
64 R. Dubey, J. Bajpai and A. K. Bajpai, *Environ. Nanotechnol., Monit. Manage.*, 2016, **6**, 32–44.
65 M. A. Hassanin, H. S. El-Gendy, M. F. Cheira and B. M. Atia, *Int. J. Environ. Anal. Chem.*, 2021, **101**, 351–369.
66 I. H. Zidan, M. F. Cheira, A. R. Bakry and B. M. Atia, *Int. J. Environ. Anal. Chem.*, 2022, **102**, 2102–2124.
67 M. A. Hassanin, S. H. Negm, M. A. Youssef, A. K. Sakr, H. I. Mira, T. F. Mohammaden, J. S. Al-Otaibi, M. Y. Hanfi, M. I. Sayyed and M. F. Cheira, *Sustainability*, 2022, **14**, 2699.
68 M. A. Hendy, T. I. Kashar, E. M. Allam, M. A. Gado, N. S. Yahia and M. F. Cheira, *ChemistrySelect*, 2024, **9**, e202402329.
69 M. E. Eissa, A. K. Sakr, M. Y. Hanfi, M. I. Sayyed, J. S. Al-Otaibi, A. M. Abdel-lateef, M. F. Cheira and H. A. Abdelmonem, *Chemosphere*, 2023, **341**, 140062.
70 T. A. Seaf Elnaser, N. F. Alotaibi, Y. H. Alruwaili, H. Gomaa, H. Sharafeldin, M. F. Cheira, H. A. Abdelmonem and M. S. Abdelrahman, *ACS Appl. Polym. Mater.*, 2025, **7**, 6348–6364.
71 A. E.-H. T. Kandil, B. M. Atia, F. M. S. E. El-Dars, M. Y. M. Hussein and M. F. Cheira, *Environ. Nanotechnol., Monit. Manage.*, 2025, **23**, 101055.
72 W. Guo, Z. Lin, K. Jiang, H. Li, X. Liang, W. An, H. Liu, H. Luo and H. Yao, *Desalination*, 2025, **600**, 118468.
73 M. A. Hendy, T. I. Kashar, E. M. Allam, M. A. Gado, N. S. Yahia and M. F. Cheira, *Mater. Today Commun.*, 2024, **40**, 109633.
74 A. E.-H. T. Kandil, B. M. Atia, F. M. S. E. El-Dars, M. Y. M. Hussein and M. F. Cheira, *J. Water Process Eng.*, 2024, **67**, 106144.
75 B. M. Atia, M. A. Gado, M. F. Cheira, H. S. El-Gendy, M. A. Yousef and M. D. Hashem, *Int. J. Environ. Anal. Chem.*, 2023, **103**, 4176–4199.
76 J. Yang, G. Qu, C. Liu, S. Zhou, B. Li and Y. Wei, *Chem. Eng. Res. Des.*, 2022, **184**, 639–650.
77 G. He, Z. Li, Y. Liu, M. Liu, C. Zhu, L. Zhang and H. Zhang, *Desalination*, 2022, **539**, 115973.
78 Z. Li, G. He, G. Zhao, J. Niu, L. Li, J. Bi, H. Mu, C. Zhu, Z. Chen, L. Zhang, H. Zhang, J. Zhang, B. Wang and Y. Wang, *Sep. Purif. Technol.*, 2021, **277**, 119519.
79 T. Ryu, Y. Haldorai, A. Rengaraj, J. Shin, H.-J. Hong, G.-W. Lee, Y.-K. Han, Y. S. Huh and K.-S. Chung, *Ind. Eng. Chem. Res.*, 2016, **55**, 7218–7225.
80 S. Wang, P. Li, W. Cui, H. Zhang, H. Wang, S. Zheng and Y. Zhang, *RSC Adv.*, 2016, **6**, 102608–102616.
81 S. M. Alshuiael and M. A. Al-Ghouti, *Sep. Purif. Technol.*, 2022, **295**, 121320.

82 S. Zhou, X. Guo, X. Yan, Y. Chen and W. Lang, *Particuology*, 2022, **69**, 100–110.
83 S. Wang, M. Zhang, Y. Zhang, Y. Zhang, S. Qiao and S. Zheng, *Hydrometallurgy*, 2019, **187**, 30–37.
84 S. Wang, P. Li, X. Zhang, S. Zheng and Y. Zhang, *Hydrometallurgy*, 2017, **174**, 21–28.
85 Y. Watanabe, K. Ohnaka, S. Fujita, M. Kishi and A. Yuchi, *Anal. Chem.*, 2011, **83**, 7480–7485.
86 C. Ai, X. Zhang, S. Xue and P.-p. Sun, *J. Environ. Chem. Eng.*, 2025, **13**, 118437.
87 B. Segura-Bailón, G. T. Lapidus and G. Ramos-Sánchez, *Miner. Eng.*, 2024, **218**, 109012.
88 L. Chen, X. Tang, Y. Zhang, L. Li, Z. Zeng and Y. Zhang, *Hydrometallurgy*, 2011, **108**, 80–86.
89 G. P. Nayaka, J. Manjanna, K. V. Pai, R. Vadavi, S. J. Keny and V. S. Tripathi, *Hydrometallurgy*, 2015, **151**, 73–77.
90 Y. Yang, S. Xu and Y. He, *Waste Manage.*, 2017, **64**, 219–227.
91 Q. Meng, Y. Zhang and P. Dong, *Waste Manage.*, 2018, **71**, 372–380.